frontiers | Frontiers in Remote Sensing

TYPE Original Research
PUBLISHED 19 December 2025
DOI 10.3389/frsen.2025.1724950

OPEN ACCESS

EDITED BY
Lei Fan,
Southwest University, China

REVIEWED BY
Mengjia Wang,
Zhengzhou University, China
Tianxiang Cui,
Nanjing Forestry University, China

*CORRESPONDENCE
Liang Wan,
liang.wan@lsce.ipsl.fr

RECEIVED 14 October 2025
REVISED 10 November 2025
ACCEPTED 18 November 2025
PUBLISHED 19 December 2025

CITATION
Wan L, Ciais P, de Truchis A, Sean E, Fischer FJ, Purnell D, Belouze G, Fayad I, Schwartz M, Xu Y, Su Y, Réjou-Méchain M, Barbier N, Tresson P, Bastin J-F, Bogaert J, Vander Linden A, Plumacker A, Angoboy Ilondea B, Assumani D-M, de Haulleville T, Sagang LB, Durieux L, Ryu Y, Yang T, Obame CV, Bossy T, Frappart F, Peaucelle M, Wigneron J-P, Chave J, Cuni-Sanchez A, Hubau W, Verbeeck H, Boeckx P, Makana J-R, Ewango C, Kearsley E, Sonké B, Libalah M and Ploton P (2025) Satellite-based mapping of annual canopy height and aboveground biomass in African dense forests. *Front. Remote Sens.* 6:1724950. doi: 10.3389/frsen.2025.1724950

Satellite-based mapping of annual canopy height and aboveground biomass in African dense forests

Liang Wan[1]*, Philippe Ciais[1], Aurélien de Truchis[2], Ewan Sean[2], Fabian Jörg Fischer[3], David Purnell[1], Gabriel Belouze[1], Ibrahim Fayad[1,2], Martin Schwartz[1], Yidi Xu[1], Yang Su[1], Maxime Réjou-Méchain[4], Nicolas Barbier[4], Paul Tresson[4], Jean-François Bastin[5], Jan Bogaert[5], Arthur Vander Linden[5], Antoine Plumacker[5], Bhely Angoboy Ilondea[6,7], Dieu-Merci Assumani[8,9], Thales de Haulleville[5,10], Le Bienfaiteur Sagang[11], Laurent Durieux[12], Youngryel Ryu[13], Tackang Yang[14], Conan Vassily Obame[15], Thomas Bossy[1,16], Frédéric Frappart[16], Marc Peaucelle[16], Jean-Pierre Wigneron[16], Jerome Chave[17], Aida Cuni-Sanchez[18,19], Wannes Hubau[10,20], Hans Verbeeck[21], Pascal Boeckx[22], Jean-Remy Makana[23], Corneille Ewango[24], Elizabeth Kearsley[25], Bonaventure Sonké[26], Moses Libalah[26] and Pierre Ploton[4]

[1]Laboratoire des Sciences du Climat et de l'Environnement, LSCE/IPSL, CEA-CNRS-UVSQ, Université Paris Saclay, Gif-sur-Yvette, France, [2]Kayrros SAS, Paris, France, [3]TUM School of Life Sciences, Ecosystem Dynamics and Forest Management, Technical University of Munich, Freising, Germany, [4]AMAP, University Montpellier, IRD, CIRAD, CNRS, INRAE, Montpellier, France, [5]TERRA Teaching and Research Centre, Gembloux Agro-Bio Tech, Université de Liège, Gembloux, Belgium, [6]Institut National pour l'Etude et la Recherche Agronomiques, Kinshasa-Gombe, Democratic Republic of Congo, [7]Université Pédagogique Nationale, Kinshasa-Ngaliema, Democratic Republic of Congo, [8]Faculté de Gestion des Ressources Naturelles Renouvelables, Université de Kisangani, Kisangani, Democratic Republic of Congo, [9]Institut National pour l'Etude et la Recherche Agronomiques (INERA - Yangambi), Yangambi, Democratic Republic of Congo, [10]Ghent University, Faculty of Bioscience Engineering, Department of Environment, Ghent, Belgium, [11]Institute of the Environment and Sustainability, UCLA, Los Angeles, CA, United States, [12]IRD, UAR Data Terra (263 IRD, 2013 CNRS, UMS 1511 INRAE), Montpellier, France, [13]Department of Landscape Architecture and Rural Systems Engineering, Seoul National University, Seoul, Republic of Korea, [14]Interdisciplinary Program in Landscape Architecture, Seoul National University, Seoul, Republic of Korea, [15]Agence Gabonaise d'Etudes et d'Observations Spatiales (AGEOS), Libreville, Gabon, [16]ISPA, UMR 1391 INRAE/Bordeaux Science Agro, Villenave d'Ornon, France, [17]CRBE, Université de Toulouse, CNRS, IRD, Toulouse INP, Toulouse, France, [18]Department of International Environmental and Development Studies (NORAGRIC), Norwegian University of Life Sciences, Ås, Norway, [19]Department of Environment and Geography, University of York, York, United Kingdom, [20]Royal Museum for Central Africa, Service of Wood Biology, Tervuren, Belgium, [21]Q-ForestLab, Department of Environment, Ghent University, Ghent, Belgium, [22]Ghent University, Faculty of Bioscience Engineering, Department of Green Chemistry, Ghent, Belgium, [23]Université de Kisangani, Faculté des Sciences, Laboratoire d'écologie et aménagement forestier, Kisangani, Democratic Republic of Congo, [24]Université de Kisangani, Faculty of Renewable Natural Resources Management, Kisangani, Democratic Republic of Congo, [25]BlueGreen Labs, Melsele, Belgium, [26]Plant Systematics and Ecology Laboratory, Higher Teachers' Training College, University of Yaoundé I, Yaoundé, Cameroon

Accurate maps of canopy height (CH) and aboveground biomass (AGB) are needed for monitoring forests over large regions. Producing such data is particularly challenging over the complex, diverse and dense humid tropical

forests of Africa where signal saturation observed from optical and radar satellites and complex responses in LiDAR data require advanced mapping techniques to capture high biomass and tall height values. Here, we trained a deep learning (U-Net) model to generate the first annual maps (2019–2022) of top CH at 10 m resolution over the African dense forest region, using Sentinel-1/-2 images trained on LiDAR-derived height data from the Global Ecosystem Dynamics Investigation mission (GEDI). To predict AGB from CH on a 30-m grid, we calibrated allometric models combining AGB data from field inventories, CH from our map, and wood density from a new high-resolution (1 km) map. The CH map has a mean absolute error (MAE) of 4.54 m and an underestimation bias of 1.54 m compared to independent airborne LiDAR data (5.93 m and 1.40 m compared to independent GEDI data). Evaluation of the AGB map against independent measurements from field sites suggests an improved accuracy (MAE = 79.65 Mg/ha, bias = 6.47 Mg/ha) compared to recent datasets such as ESA-CCI, NCEO, and GEDI L4B. Our map also captures the large-scale spatial gradients of AGB across African dense forests, as observed in a comprehensive dataset of forest concession measurements aggregated at a 1-km scale. Interpretable machine learning was used to assess the contribution of ancillary variables (e.g., climate, soil, forest type) to biomass prediction. While some variables were relevant, their inclusion failed to improve AGB estimates in high and low biomass extremes and introduced spatial artifacts, limiting their utility for consistent annual mapping. Together, our annual CH and AGB maps offer an open, scalable tool for monitoring forest disturbances and interannual biomass dynamics. Future work will focus on refining biomass–height relationships to further improve AGB estimation.

KEYWORDS

forest height, aboveground biomass, African dense forests, GEDI, Sentinel-2, Sentinel-1, deep learning, allometric relations

1 Introduction

Accurate mapping of forest canopy height (CH) and aboveground biomass (AGB) is fundamental for quantifying carbon stocks and assessing the impacts of disturbances in tropical ecosystems (Chave et al., 2014; Duncanson et al., 2022; Réjou-Méchain et al., 2019). However, obtaining consistent and high-resolution estimates remains challenging due to limited field measurements, the spatial heterogeneity of forests, and persistent cloud cover in tropical regions (Bossy et al., 2025). These challenges are particularly acute in Africa, where data availability has long lagged behind other tropical forest regions. The African dense forest biome, which contains approximately 10% of global forest carbon stocks (Pan et al., 2024; Xu et al., 2021), plays a vital role in maintaining the global ecological balance by supporting biodiversity and regulating the water cycle (Fan et al., 2019; Raven et al., 2020). Despite its importance, this biome has undergone widespread deforestation and degradation over recent decades (Hansen et al., 2013; Curtis et al., 2018; Vancutsem et al., 2021), and estimates of its carbon balance remain highly divergent (Ciais et al., 2011; Valentini et al., 2014; Zhao et al., 2024). Resolving these discrepancies requires spatially explicit and temporally consistent monitoring of CH and AGB. In particular, such monitoring is crucial for detecting carbon emissions from processes like selective logging, slash-and-burn agriculture, and peat swamp forest degradation (Crezee et al., 2022; Zhao et al., 2024).

CH and AGB measurements rely on field inventories measuring individual trees, and airborne and terrestrial Light Detection and Ranging (LiDAR) covering small areas (Nelson et al., 1997; Wang et al., 2019). National Forest Inventories (NFI) and research plots (e.g., AFRITRON [https://afritron.org/]) have provided invaluable insights but upscaling these data to countries or regions is a particular challenge (Fassnacht et al., 2024; McRoberts et al., 2024). Furthermore, field measurements of CH and AGB come from different plot sizes and use different sampling methods (Réjou-Méchain et al., 2019). Airborne LiDAR (ALS) data, although effective for estimating CH and AGB over larger areas than field inventories, cannot be frequently updated due to high acquisition costs and practical constraints such as restricted flight schedules, unfavorable weather, and challenging topography (Xu et al., 2017; Rodda et al., 2024; Sagang et al., 2024). Today, major gaps remain in the availability of tropical African forests CH and AGB ground data, despite considerable efforts to improve field data collection.

Advances in satellite remote sensing improve the prospects for forest CH and AGB monitoring. Spaceborne LiDAR systems, such as the Geoscience Laser Altimeter System (GLAS) aboard the Ice, Cloud, and land Elevation Satellite (ICESat) platform, have facilitated the development of forest CH data by using MODIS products and various ancillary variables (Simard et al., 2011; Tao et al., 2016; Wang et al., 2016). GEDI L2A data (Dubayah et al., 2020a) providing better CH than ICESat (Neuenschwander and Pitts, 2019) over dense forests, with a potential for retrieving AGB (Liu et al., 2021; Zhu et al., 2022). Additionally, Landsat satellite imagery has been applied to fill gaps in the spatial coverage of sparse GEDI samples by Potapov et al. (2021) to generate the first global 30-m CH map. The availability of Sentinel-2 at a 10-m resolution and the synergistic use of Sentinel-1/-2 have enhanced the accuracy of

CH mapping (Lang et al., 2023; Schwartz et al., 2023; Fayad et al., 2024; Pauls et al., 2024; Schwartz et al., 2024) by leveraging cloud-penetrating synthetic aperture radar (SAR) data and frequent optical observations, thereby reducing data gaps caused by persistent cloud cover and improving the characterization of canopy structure. Yet, a previous application of this approach by Pauls et al. (2024) showed a large underestimation of CH in dense tropical forests.

Data coverage, detail, and accuracy for CH and AGB retrieval remain challenging for monitoring African dense forests (Ploton et al., 2020), due to several factors. (1) Lack of robust high-resolution CH models: Effective prediction of CH in dense forests is hindered by the scarcity of reliable, high-quality, remotely-sensed training datasets, particularly in areas with tall and dense canopies. CH models based solely on optical imagery such as Sentinel-2 and Landsat may be influenced by saturation effects, leading to uncertainties and underestimations of tall forest heights (Pourshamsi et al., 2021; Lang et al., 2023). (2) Complexity of CH-AGB allometry relationships at the scale at which AGB is predicted from remote sensing methods (typical pixels of 30–100 m): CH-AGB allometric relationships vary across forest types and structures, and reflect disturbance history and environmental conditions, which requires extensive field data to calibrate robust models. In addition, matching AGB values with satellite-derived CH is challenging when the measurements are taken several years apart, because trees may grow, die, or be disturbed during that time. This temporal mismatch has been partly overlooked in previous studies (Duncanson et al., 2019). Furthermore, the relationship between AGB and CH is influenced by covariates such as canopy cover, soil properties and climate, which are only available at coarse spatial resolution and are less reliable in dense African forests (Fassnacht et al., 2021; Jha et al., 2021; Liang et al., 2023; Sagang et al., 2024). Additionally, while global and regional AGB maps are available (see details in Section 2.4.3), their spatial resolution (100 m–1 km) is too coarse to capture small-scale heterogeneity (e.g., local disturbances), and most provide estimates for only a single reference year. However, understanding forest dynamics and degradation processes in tropical regions requires temporally consistent and spatially detailed monitoring. Most existing CH and AGB products do not offer such annual continuity.

To address these gaps, we present a scalable approach for producing annual 10-m CH and 30-m AGB maps over African dense forests from 2019 to 2022. Our model, trained on multi-year GEDI LiDAR and Sentinel-1/-2 data, incorporates consistent pre-processing, strict quality filtering, and year-specific inference to ensure temporal consistency and spatial generalization. The resulting products enable the tracking of forest structure dynamics, offering an operational solution for fine-scale carbon monitoring and forest disturbance assessment across the region. The objectives of this study are: (1) to develop a robust deep learning framework for annual CH mapping over dense tropical African forests, mainly lowland forests, incorporating a strict sample selection in the training datasets; (2) to perform multi-scale validations of annual CH maps using independent GEDI data, ALS data, and field inventories; (3) to build new regional allometric CH-AGB models trained using a large collection of field-measured AGB data and validated against independent field data; (4) to produce annual AGB maps in African dense forests and compare the performance with various published biomass product; and (5) to explore the potential of detecting interannual changes in CH and AGB using the generated annual maps. Our CH dataset at 10 m and AGB dataset at 30 m resolution is called 'FORest Multiple Source for Africa" (FORMS-Africa V1) and covers the period 2019–2022. We generated the AGB map at 30 m resolution, rather than the 10 m resolution used for CH, to match the scale of most field plots (≥30 m) and the typical crown size of large tropical trees (~20 m), thereby minimizing uncertainty between ground measurements and satellite data (Duncanson et al., 2025). Note that our current study focuses specifically on African dense forests, which are predominantly lowland; approximately 93% of the area lies below 800 m elevation. In future updates, coverage will be expanded to include additional forest types, including montane forests.

2 Materials and methods

2.1 Satellite data sources

The deep learning model proposed in this study for CH estimation uses Sentinel-1 SAR, Sentinel-2 L2A and GEDI RH100 data in African dense forests. Sentinel-2 imagery provides multispectral information related to forest canopy structure but is highly susceptible to cloud cover, particularly in tropical forests. In complement, Sentinel-1 offers robust Synthetic Aperture Radar (SAR) data that is not dependent on daylight and less affected by weather conditions than multispectral images except in presence of large raindrops in convective clouds, and can capture forest growth dynamics (Ygorra et al., 2021). The GEDI RH100 data were used as target CH data for model training, based on the GEDI L2A RH100 products (V002) (Dubayah et al., 2020b). RH100 was selected as a proxy for the dominant canopy height (top height) within the 25-m GEDI footprint, consistent with its intended biophysical interpretation (Qi and Dubayah, 2016). In dense tropical forests, where tall emergent trees are common, RH100 better captures the full vertical extent of the canopy structure. While RH95 or RH98 may reduce sensitivity to waveform noise, they tend to systematically underestimate maximum CH, particularly in forests with complex vertical stratification when compared with ALS data (Potapov et al., 2021; Lang et al., 2023). Moreover, RH100 has been adopted in recent large-scale CH mapping efforts (e.g., Pauls et al., 2024; Zhu et al., 2022), providing consistency and comparability with prior studies. The uncertainty in RH100 has also been significantly reduced in the second release of GEDI data (R02) (Tang et al., 2023). To further mitigate noise, we applied an additional quality filtering procedure to the RH100 observations prior to model training (Section 2.2.2).

Sentinel-1 SAR data were downloaded via the public bucket (https://registry.opendata.aws/sentinel-1/). We utilized Sentinel-1 Level-1 Ground Range Detected (GRD) products acquired in Interferometric Wide (IW) swath mode at a 10-m resolution (https://docs.sentinel-hub.com/api/latest/data/sentinel-1-grd/) (Torres et al., 2012), and obtained images for each localization at nearly the same time, regardless of weather conditions or daylight. The Sentinel-1 constellation includes two satellites, S1A and S1B, but S1B terminated in January 2022, bringing a gap of coverage in the south-eastern region of the Central African Republic. In this study, we used only the VH polarization band from Sentinel-1

imagery to minimize feature redundancy and computational complexity. This choice is supported by previous research (Silveira et al., 2023; Schwartz et al., 2024), which demonstrated that VH is more sensitive than VV to forest structural parameters such as CH, diameter at breast height, and wood volume, especially in tall forests where the VV signal tends to saturate. Our results also confirmed that VH exhibits stronger sensitivity to CH changes than VV (Supplementary Figure S1), supporting its use as the main backscatter input.

Sentinel-2 L2A data were generated from Sentinel-2A/-2B after atmospheric correction using the Sen2Cor algorithm. To reduce input data dimensions, we selected all 10-m resolution wavebands, including three visible wavebands (B02, B03, B04) and a near-infrared (NIR) waveband (B08). Additionally, we included the 20-m shortwave infrared band (B11, SWIR 1), resampled to 10 m using bilinear interpolation, due to its capacity to capture water absorption features and its higher sensitivity to vegetation structure compared to another shortwave infrared band (B12, SWIR 2) (Wan et al., 2024). This characteristic makes the B11 band valuable for monitoring forest height and biomass (Astola et al., 2019; Fassnacht et al., 2021). Thus, a total of six bands were used for model training and prediction.

2.2 Pre-processing of sentinel-1/-2 and GEDI data

2.2.1 Sentinel-1/-2 data pre-processing

To retain high-quality Sentinel-1/-2 data, within each tile of size 20 × 20 km, firstly, we processed Sentinel-1 GRD products using radiometric terrain calibration (Small, 2011), orthorectification, and border noise removal. Secondly, we generated a temporal stack of Sentinel-1 imagery by selecting the 10 images captured during the main dry season (June to October) with the lowest mean backscatter, aiming to reduce the influence of residual rainfall or surface moisture. This selection improves the signal-to-noise ratio and enhances the contrast between vegetation and bare soil, ensuring more consistent and dry-condition observations for analysis. This approach also helps ensure temporal consistency across years when constructing multi-year composites. Thirdly, we calculated the temporal mean of the stack to reduce radar noise and scaled the resulting mean composite values between 0 and 1. The Sentinel-2 L2A data were filtered by selecting only images acquired during the driest months of the year, each tile being cropped to align with the grid of Sentinel-2 raw products. We utilized the cloud mask provided by the European Space Agency (ESA) to select the three least cloudy Sentinel-2 images. For products with identical cloud cover, we prioritized those with the lowest mean water vapor content, using the water vapor content sub-product delivered by ESA. This step effectively minimizes impacts from 'heavy atmospheres' with opaque clouds, cirrus, and haze. Finally, Sentinel-2 images were normalized to a range of 0–1 across all spectral bands.

2.2.2 GEDI data pre-processing and collocation with sentinel pixels

To match GEDI and Sentinel-1/-2 data, we processed GEDI L2A footprints from 2019 to 2022 by applying a series of quality control criteria (Dubayah et al., 2020b). Specifically, we retained footprints with a quality_flag of 1 to exclude invalid waveforms, and applied num_detectedmodes >0 to remove noisy returns lacking canopy signal. For model fine-tuning, we applied stricter spatiotemporal filtering: only full-power beams (fullpower_beam = 1) were used, and footprints were limited to those acquired within ±6 months of the corresponding Sentinel-1/-2 image dates to improve temporal consistency. Full details of the two-phase training strategy are provided in Section 2.3.3. GEDI RH100 values were rasterized by assigning each footprint to the 10 m Sentinel-1/2 pixel that contains its center, following a center-based collocation approach recommended by Schwartz et al. (2024). Despite the mismatch between GEDI's 25 m footprint and the 10 m Sentinel pixel size, this method yields better results than using a 20 m resolution match.

2.3 Model framework for canopy height and biomass estimation

The framework for CH and AGB estimation and validation, is presented in Figure 1. Firstly, we developed a deep learning model framework for mapping CH at 10 m resolution, and compared the results with existing global CH products and reference datasets. In order to improve the accuracy of CH retrieval, we designed a rigorous sample selection strategy (Section 2.3.2), using Sentinel-1/-2 as model inputs and quality-filtered GEDI RH100 as the target variable. This strategy aims to reduce saturation effects in tall forests and the ubiquitous presence of clouds in the study region. Secondly, we produced an ensemble of five AGB maps from the CH map (AGB1–5, Section 2.4.3) based on different CH-AGB allometric models using parametric equations, parametric equations combined with machine learning, and pure machine learning models. These allometric models are calibrated using field inventory AGB and modelled CH, wood density (WD), and ancillary data as covariates (Section 2.4.3). Finally, we evaluated the AGB maps using independent inventories from many forest concessions in Central Africa aggregated at 1 km scale (Ploton et al., 2020). Regrowth and degradation that happened between the date of those inventories and the recent years of our AGB retrieval are used to interpret the differences between inventories and our maps.

2.3.1 Canopy height model

The U-Net model architecture (Ronneberger et al., 2015), a fully convolutional neural network (CNN), was used to perform a pixel-wise regression of GEDI RH100 from Sentinel-1/-2 images. We chose a U-Net architecture because it is well-suited for dense prediction, offering improved speed and accuracy over previous models while requiring fewer training examples (Ronneberger et al., 2015). The encoder–decoder architecture of the U-Net, combined with skip connections, allows the model to effectively capture both broad spatial context and fine-grained local details, which is essential for accurately predicting sub-pixel forest structure from high-resolution satellite imagery (Schwartz et al., 2024; Wagner et al., 2025). In previous work, we explored advanced architectures such as Transformers for high-resolution CH mapping over small regions (Fayad et al., 2024; Fogel et al., 2025). While these models achieved strong performance, they involve greater complexity and computational demands. In contrast, the U-Net is substantially simpler yet delivered comparable performance in our experiments.

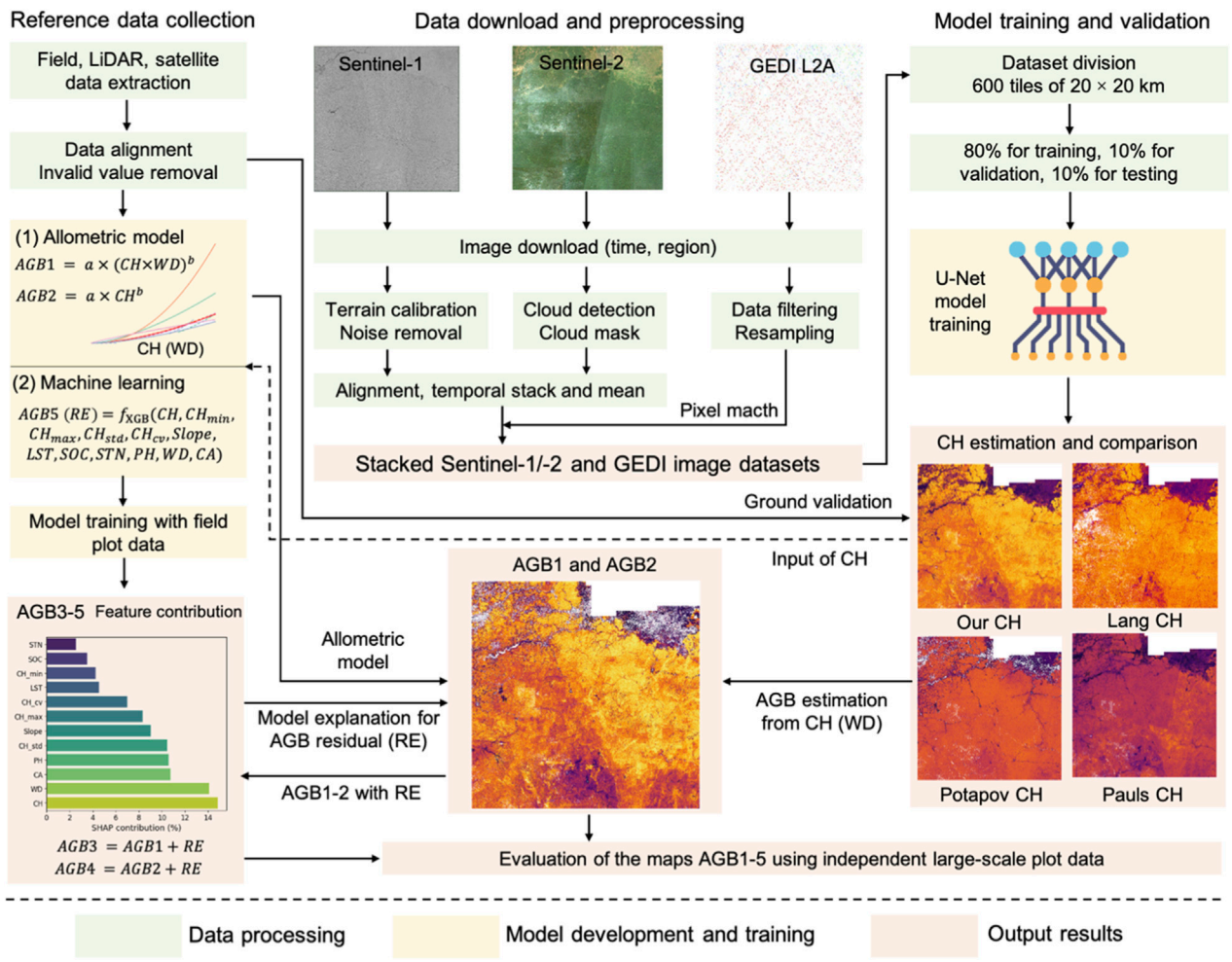

FIGURE 1
Framework for canopy height (CH) and aboveground biomass (AGB) estimation. The primary steps include reference data collection, satellite data download and processing, CH model training and validation, and AGB model development and validation. Based on modeled CH, a global wood density map, and various ancillary data, we produced five AGB maps (AGB1–5) using parametric allometric, hybrid, and machine learning approaches.

To train the U-Net model (Supplementary Figure S2), Sentinel-1/-2 images were used as model inputs, while GEDI RH100 served as training labels, available only for specific locations and dates. Each training sample comprised 6 bands (1 Sentinel-1 and 5 Sentinel-2) extracted over a 256 × 256 pixel image patch. The U-Net model processes images through multiple layers, progressively extracting more complex features at each stage. Once trained, the model was used to generate annual CH maps at a 10-meter resolution across the entire dense forest region of Africa. A detailed description of the training datasets and model training process is provided in Sections 2.3.2 and 2.3.3. Although previous studies, such as Lang et al. (2023), demonstrated the potential of deep learning for CH mapping using GEDI data, their use of deep convolutional neural networks differed from classical encoder-decoder architectures such as U-Net, which we adopt for their strength in preserving spatial detail. Importantly, accurate CH mapping remains an open challenge. Recent models, including the product by Lang et al. (2023), still show notable limitations in performance, as demonstrated in comparative evaluations (Moudrý et al., 2024). In our study, we adopt a U-Net-based architecture and tailor it to address the specific challenges of annual CH monitoring, which remain insufficiently explored in existing literature. We introduce three key innovations: (1) incorporating Sentinel-1 SAR data to reduce cloud-related gaps and potentially alleviate saturation in CH estimates, whereas Lang et al. (2023) only used Sentinel-2 data; (2) using a minimal and consistent set of six input bands to ensure transferability across years and regions; and (3) training year-specific models to produce temporally consistent annual CH maps across the dense forests of Africa. To evaluate the contribution of Sentinel-1, we conducted a regional comparison in Gabon using the same U-Net architecture, trained once with and once without Sentinel-1 input. The results (Supplementary Figures S3, S4) show that incorporating Sentinel-1 improves spatial detail and reduces saturation effects in tall forest areas compared to the S2-only model. This suggests that radar-derived contextual information may help the model better reproduce CH patterns from Sentinel-2 imagery. However, we acknowledge that the overall improvement compared to Lang et al. (2023) may also result from differences in model framework, not just the inclusion of Sentinel-1 data. A broader-scale quantitative assessment of Sentinel-1's contribution remains an important direction for future work.

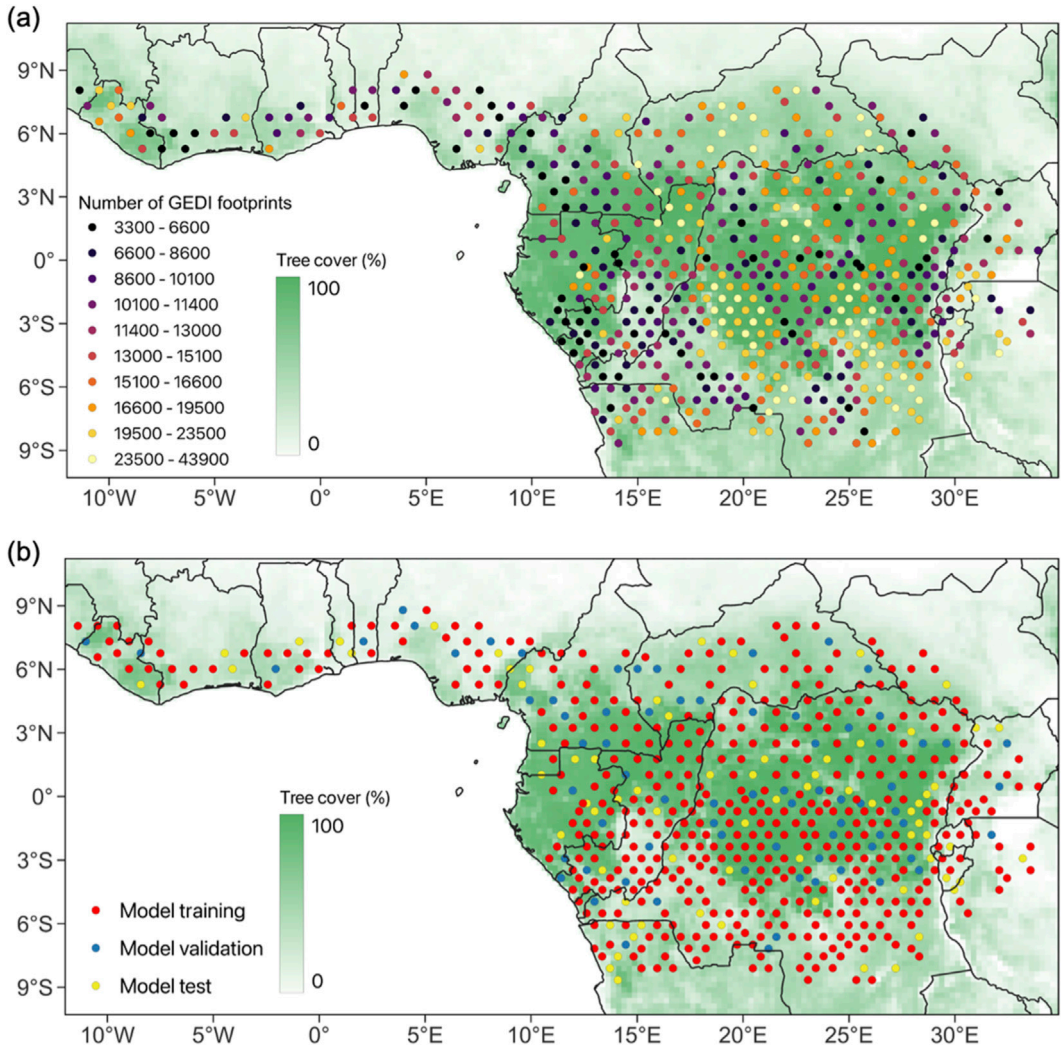

FIGURE 2
Number **(a)** and spatial distribution of the number of GEDI footprints within the tiles of 20 × 20 km (points with varying colors). **(b)** of GEDI footprints used for model training (red), validation (blue), and testing (green). The tree cover map was derived from the Global Forest Change dataset developed by Hansen et al. (2013) and aggregated to a resolution of 0.25°.

These adaptations enable scalable, time-resolved, and cloud-resilient monitoring for annual CH mapping, and have already supported the generation of 30 m resolution operational annual forest biomass products, which had not been achieved in previous studies (Potapov et al., 2021; Lang et al., 2023).

2.3.2 Construction of training datasets

The U-Net model was trained on Sentinel-1/-2 and GEDI data from 600 largely non-overlapping 20 × 20 km tiles covering the African dense forest region (Figure 2). The tiles were evenly distributed across the study area and selected to maximize the number of GEDI orbits within each tile. For each tile and year, we selected the three least cloudy Sentinel-2 images. When sampling the batch, we randomly selected Sentinel-2 images for the forward pass during training and performed inferences with at least 3 Sentinel-2 images of the year and calculated their temporal median to produce the final CH map. The final training dataset used during the fine-tuning phase (Section 2.3.3) comprises 8.5 million GEDI footprints after applying quality filters. In our study region, more than 80% of available GEDI shots were excluded due to stricter quality criteria, primarily because of cloud contamination, geolocation errors, and low waveform quality. These issues are particularly frequent in tropical forests with dense vegetation. The number of selected GEDI footprints is shown in Figure 2a. To ensure spatial independence between training and evaluation, we randomly assigned entire tiles to one of three mutually exclusive subsets: 480 tiles (80%) for training, 60 tiles (10%) for validation, and 60 tiles (10%) for testing (Figure 2b). While a small degree of edge overlap exists between some neighboring tiles, this tile-based partitioning substantially reduces spatial autocorrelation and prevents direct pixel-level leakage between subsets. To increase sample diversity and reduce overfitting, we applied data augmentation through (1) random 256 × 256 crops from the 600 tiles, (2) random horizontal and vertical flips and ±90° rotations, and (3) random selection of the acquisition year (2019–2022) for each tile during each training epoch, ensuring temporal diversity.

2.3.3 Model training and prediction

We iteratively optimized the U-Net model's loss function by minimizing the difference between estimated and GEDI observed height data. Unlike conventional regression losses such as mean absolute error (MAE) or mean squared error (MSE), we chose to use a weighted version of the MAE, inspired by Lang et al. (2023), in order to balance the weight of each height class and more properly handle the tails of the height distributions (low and high trees). To do so, for each zone, the number of GEDI footprints for each 1-meter height bin was computed, and their corresponding weight is the square root of the inverse of their relative frequency. During training, tiles were randomly drawn according to their weights so that tiles with larger weights were drawn more often. Each training batch consisted of 20 input images of size 256 × 256 pixels, incorporating pre-processed Sentinel-1/-2 images and corresponding GEDI labels for pixels with available footprints. The U-Net model was initialized with random weights (no pre-training or fine-tuning) and trained in two phases. In the first phase, the model was trained for 300 epochs, with an epoch size consisting of 25 batches (batch size of 20 images, covering ~500 tiles per epoch), and an initial learning rate of 0.008. Batches were sampled with replacement, ensuring diversity in each epoch while following a standard convention for updating training metrics and adjusting the learning rate. The learning rate was halved if the validation loss did not improve for 20 consecutive epochs. This phase used all GEDI RH100 footprints that passed the basic quality filters (quality_flag = 1 and num_detectedmodes >0), without constraints on acquisition date or beam type. In the second phase, we resumed training from the model's previous state and trained for an additional 200 epochs using a cyclic learning rate ranging from 10^{-5} to 5×10^{-4}. This fine-tuning phase employed a more restrictive subset of GEDI data: only full-power beam footprints acquired within ±6 months of the Sentinel-2 image acquisition date were used, to improve spatiotemporal alignment between training labels and inputs. This final phase aimed to fine-tune the model with high-quality labels for improved accuracy.

The entire African dense forest region was subdivided into 23,781 tiles for the CH inference. For each year and Sentinel-2 tile, three cloud-free images within a ±6-month window of GEDI acquisition were selected. Inference was conducted separately on each image, and the final annual prediction was obtained by taking the temporal median of the three results. This approach helps mitigate the effects of short-term variability such as residual clouds, seasonal differences, and local disturbances, and reduces the potential impact of temporal mismatch between GEDI and Sentinel-2 observations. While abrupt changes such as fire or shifting cultivation may occur in some areas, they represent a small fraction of the region, and the aggregation strategy helps ensure robust annual-scale biomass estimates. A subsequent workflow was then triggered to merge the individual tiles into Cloud Optimized GeoTIFF files, creating a comprehensive CH map for the entire African dense forests.

2.3.4 Canopy height comparisons and validation

We compared the CH maps against unseen RH100 data from GEDI, top canopy height from ALS, and previous satellite-derived height maps.

1. GEDI validation: The CH maps were validated against GEDI RH100 footprints from the test dataset, randomly selected across the African dense forests for all the years under consideration (the test set shown in Figure 2).
2. Airborne LiDAR validation: We further validated the CH maps using over 140 ALS acquisitions, covering 32,000 ha (Figure 3d), which were obtained from published studies (Xu et al., 2017; Rodda et al., 2024). We also evaluated the CH map using two recently collected ALS datasets from the Luki Biosphere Reserve (November 2023) and the Yangambi Biosphere Reserve (October 2023) in the DRC. A detailed description of these two ALS datasets is provided in Supplementary Text 1. To ensure consistency with our CH maps, the ALS CH data were resampled by taking the maximum value of 1 m raster data within each output pixel and compared with CH maps derived in this study from the closest mapping year. We used the forest mask derived from the Global Forest Change dataset developed by Hansen et al. (2013) to exclude non-forest pixels.
3. Comparison with global height products: Finally, our CH map (10 m; RH100) was also compared with the map of Lang et al. derived from Sentinel-2 and GEDI-RH98 (10 m) in 2020 (Lang et al., 2023), the map of Potapov et al. from Landsat imagery and GEDI-RH95 for the year 2019 at 30 m resolution (Potapov et al., 2021; Potapov et al., 2022), and the map of Pauls et al. from Sentinel-1/-2 imagery and GEDI-RH100 in 2020 at 10 m (Pauls et al., 2024). For visual comparisons, we used our CH map from 2019.

2.4 Development and validation of AGB maps

2.4.1 Field measurement data

To develop allometric models deriving AGB from CH, we collected reference in-situ AGB data from various sources across Africa (Table 1; Figures 3a–c). We averaged our modeled CH across all 10 m pixels within the known boundary of each inventory plot. For matching our CH maps to ALS data, we extracted CH pixels within each flight coverage with a buffer of 20 m for excluding edges. For data from the Central African plot network (https://cafriplot.net/network) and AfriSAR datasets (Labriere et al., 2018), only the Lorey height (LH) within each plot was available. Since our CH model estimates maximum canopy height rather than LH, we applied a linear regression conversion (CH = 0.7133 × LH + 16.1777), derived from these two datasets (Supplementary Figure S5). The relationship between LH and CH was found to be approximately linear across the observed range, supporting the use of this transformation. Although a nonlinear model yielded a slightly higher correlation, this was largely influenced by a few outlying points with higher uncertainty and saturation that deviated from the main trend. The probability density of field-measured AGB collocated with our modeled CH data is shown in Supplementary Figure S6.

2.4.2 AfriSAR LVIS LiDAR-derived AGB data

We evaluated our AGB map using LiDAR-derived AGB from AfriSAR campaigns in Gabon (Armston et al., 2020) acquired by

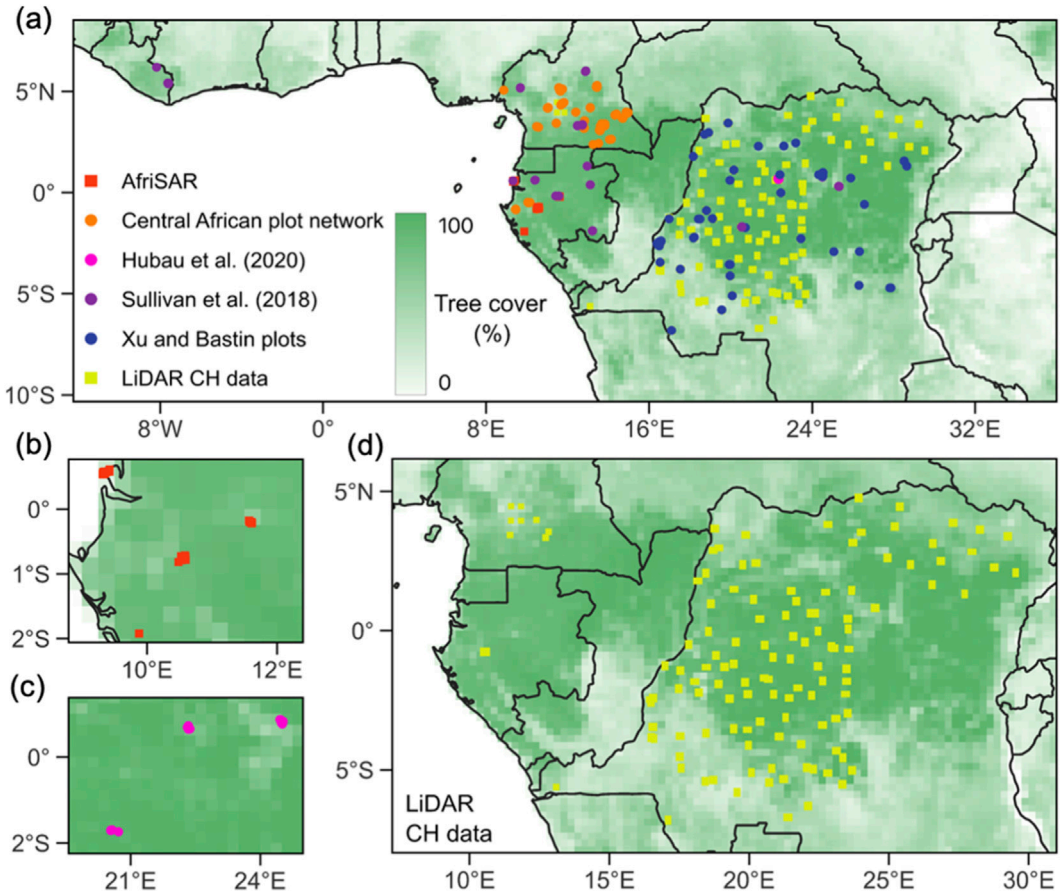

FIGURE 3
Spatial distribution of field inventories plot and airborne LiDAR (ALS) data for canopy height and/or aboveground biomass measurements. **(a)** Distribution of all data points. **(b,c)** Detailed distribution of overlapping data points from the AfriSAR and Hubau et al. (2020) datasets. **(d)** Distribution of all ALS data. Each ALS sampling region was represented by its four corner coordinates. Field plot and ALS data were represented by circles and squares, respectively, in different colors. The tree cover map was derived from the Global Forest Change dataset developed by Hansen et al. (2013) and aggregated to a resolution of 0.25°.

TABLE 1 Summary of canopy height (CH) and aboveground biomass (AGB) from field plot and airborne LiDAR (ALS) data.

Data source	Variable	Region	Time	Field scale
AfriSAR data (Saatchi et al., 2019)	CH, AGB	Gabon	2016	0.16, 0.25, 1 ha
Central African plot network	CH, AGB	Gabon, Cameroon	2012–2023	Plot (1 ha)
Hubau et al. (2020)	CH, AGB	DRC	2011–2015	Plot (1 ha)
Sullivan et al. (2018)	CH	Central Africa	—	Tree level in 30-m radius
Xu and Bastin plots (Chave et al., 2014; Xu et al., 2017)	CH, AGB	DRC	2014	Plot (1 ha)
Airborne LiDAR CH (Xu et al., 2017; Rodda et al., 2024)	CH	Central Africa	2012–2023	20 m

NASA's Land, Vegetation, and Ice Sensor (LVIS) instrument during 2016. The AfriSAR LVIS reference AGB dataset was estimated by Armston et al. (2020) using an allometric model (Equation 1) incorporating canopy top height, stand basal area density (BAD) and wood density (WD):

$$AGB = CH^{a} \times BAD^{b} \times WD^{c} \quad (1)$$

Note that the AfriSAR LVIS dataset estimated AGB used a regional mean WD from Chave et al. (2009) that may not fully capture the real value. Here, we selected the LVIS AGB maps from the Mabounié, Mondah, and Lopé sites (Labriere et al., 2018), with a resolution of 50 m. To ensure a consistent comparison between our AGB estimates and LVIS, we excluded non-forest pixels from both datasets before analysis using the forest cover mask from Hansen et al. (2013).

TABLE 2 Summary of five aboveground biomass (AGB) maps based on different allometric methods and input variables. Details of the ancillary data are provided in Supplementary Table S2.

Allometric model name	Source	Input variable (CH is from our satellite data)
AGB1	Parametric model (Equation 2) fitting CH-AGB relationship with field AGB and our satellite-based CH	CH
AGB2	Parametric model (Equation 3) fitting CH × WD and AGB relationship with field AGB, our satellite-based CH and WD.	CH, WD
AGB3	Hybrid parametric and machine learning model that follows AGB1 in a first step, and simulates the residuals between measured AGB and estimated AGB1 using an XGBoost model (trained with ancillary data) in a second step	CH, WD, ancillary data
AGB4	Hybrid parametric and machine learning model same than AGB3 but the first step is the AGB2 model	CH, WD, ancillary data
AGB5	Pure machine learning model (XGBoost) trained with CH, WD, and ancillary data to fit field AGB	CH, WD, ancillary data

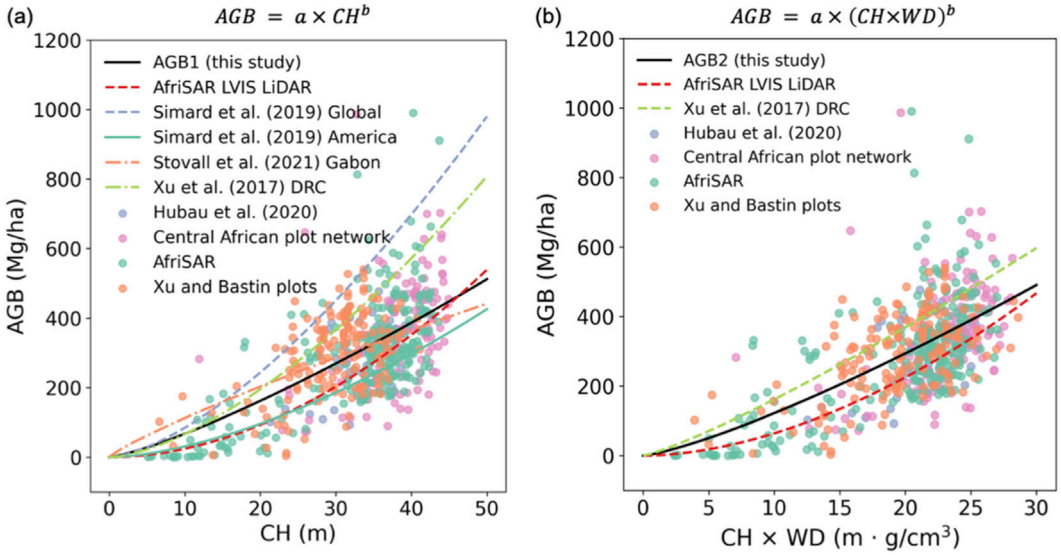

FIGURE 4
Allometric relationships between aboveground biomass (AGB) and canopy height (CH). **(a)** AGB1 model based on Equation 2. **(b)** AGB2 model on Equation 3 which includes wood density (WD) as well as CH. The specific regression parameters are calibrated using 80% of the total field samples from Table 1.

2.4.3 Modeling and validation of aboveground biomass

We used field plot and the above mentioned LVIS LiDAR AGB estimates (Table 1) along with our CH maps and WD maps to calibrate different allometric models of parametric, hybrid, and machine learning types, and generate an ensemble of five AGB maps at 30 m resolution (AGB1–5, Table 2). The mapping accuracy of each map was evaluated against independent 1 km scale forest concessions inventories covering nearly 100,000 ha in Central Africa (Ploton et al., 2020).

Parametric AGB estimation models (AGB1 and AGB2): These parametric models are given by Equation 2 and Equation 3 (Xu et al., 2017; Simard et al., 2019; Stovall et al., 2021):

$$AGB1 = a \times CH^b \quad (2)$$

$$AGB2 = a \times (CH \times WD)^b \quad (3)$$

where the independent variable is WD extracted from the global map of Fischer et al. (2025) (see Supplementary Text 2). Note that we use our modelled CH averaged at each field site, instead of field-measured CH, because in the end, the fitted relationships (2) and (3) are used for mapping AGB using modelled CH maps. We applied cross-validation by using 80% of the total samples from Table 1, the remaining 20% reserved for validation (Supplementary Figure S7). The AGB1 calibrated model is $AGB = 3.7412 \times CH^{1.2573}$, and the AGB2 model is $AGB = 6.5981 \times (CH \times WD)^{1.2670}$. The results are displayed in Figure 4 below. We verified that fitting these models using field-measured CH instead of modelled CH gave similar curves (Supplementary Text 3, Supplementary Figure S8). We also examined six model variants of Equation 2 and three

variants of Equation 3, calibrated using different combinations of field plot and LVIS LiDAR data, and using only LVIS data (see Supplementary Table S1). Models used in previous studies for tropical dense forests are shown in Figure 4 for information (Xu et al., 2017; Simard et al., 2019; Stovall et al., 2021).

Hybrid AGB estimation models (AGB3 and AGB4): We used residual modeling to evaluate whether machine learning could reduce or explain the remaining errors from the initial parametric models. Specifically, we first applied the parametric models (Equations 2,3) to estimate AGB (AGB1 and AGB2). In a second step, we applied a non-parametric XGBoost model (Chen and Guestrin, 2016) to model the residuals, defined as the differences between measured AGB and the initial parametric fit predictions (Equation 4). This two-step approach aimed to capture complex patterns not accounted for by the parametric relationships. The XGBoost model is defined by:

$$RE = f_{XGB}(CH, CH\_min, CH\_max, CH\_std, CH\_cv, Slope, LST, SOC, STN, PH, WD, CA) \quad (4)$$

where RE is the residual representing the difference between measured AGB and AGB1 or AGB2. The factors assumed to influence RE are (see Supplementary Table S2): (1) Forest structural attributes: CH_min, CH_max, CH_std, and CH_cv, the minimum, maximum, standard deviation, and coefficient of variation of our satellite-derived CH data across the nine 10 m CH pixels that compose each 30 m AGB pixel, WD, and CA defined by the score of the first axes of a correspondence analysis (CA) performed on the predicted abundances of 193 tree taxa by Réjou-Méchain et al. (2021); (2) Environmental and climatic factors: Slope calculated from NASA SRTM Digital Elevation (Farr et al., 2007), LST the land surface temperature from Landsat-8 (Jimenez-Munoz et al., 2014); (3) Soil properties: STN, SOC, and PH are soil total nitrogen, organic carbon, and pH, respectively (Hengl et al., 2021). CA and WD are at 10-km and 1-km resolutions, respectively, and other datasets are at 30 m resolution. Similar to the calibration of the parametric models, we randomly selected 80% of the total dataset to train the RE model, the remaining 20% used for cross validation. We produced residual (RE) maps for AGB1 and AGB2, which gave the AGB3 and AGB4 maps (Equations 5, 6):

$$AGB3 = AGB1 + RE \quad (5)$$

$$AGB4 = AGB2 + RE \quad (6)$$

Machine learning AGB estimation model (AGB5): This model directly employed the XGBoost model to fit AGB (Equation 7) using modelled CH and ancillary data as given by:

$$AGB5 = f_{XGB}(CH, CH\_min, CH\_max, CH\_std, CH\_cv, Slope, LST, SOC, STN, PH, WD, CA) \quad (7)$$

The performance of the five AGB-CH models were evaluated using R^2, MAE, RMSE, and Bias. We found that the hybrid and pure machine learning models were prone to overfitting and did not outperform the parametric models in mapping accuracy, primarily due to limited and low-quality training data. These models also exhibited spurious spatial patterns—or "hallucinations"—likely driven by the coarse spatial resolution and limited predictive value of several input variables, particularly climate and soil features. As a result, the residual-based models (AGB3 and AGB4) displayed less reliable spatial structures compared to the parametric models. These limitations and their impacts are discussed in detail in Supplementary Text 4, Sections 3.3, 3.4. Therefore, we present results for AGB1 and AGB2, which are compared with other AGB products listed in Table 3. We applied SHapley Additive exPlanations (SHAP) (Lundberg, 2017) to analyze the contributions of CH and other variables to the estimation uncertainty (RE) in AGB1 and AGB2.

We also evaluated the AGB1 and AGB2 maps, as well as our three other maps (Table 2) against an independent, large-scale 1-km AGB in-situ dataset aggregated from nearly 100,000 ha of Central African forests (Ploton et al., 2020) hereafter called AGB-P. The AGB-P dataset was aggregated from extensive *in situ* forest concessions inventories conducted between 2000 and the early 2010s across five countries. To get better insights on the differences between our maps and the AGB-P data that were collected many years before, we investigated the impact of the lag between the date of our map and the date of collection of AGB-P by calculating the time of forest regrowth since each degradation event observed in the AGB-P areas. Information on forest regrowth and degradation was derived from the Tropical Moist Forest (TMF) historical disturbance dataset of Vancutsem et al. (2021), with specific details provided in Supplementary Text 5. Finally, we explore the potential of detecting interannual changes in CH and AGB using the generated annual maps, guided by disturbance information from the TMF map (Supplementary Text 6). All comparisons were evaluated using the correlation coefficient (R^2), MAE, root mean square error (RMSE), and Bias.

3 Results

3.1 Validation and comparison of canopy height model

Our deep learning model demonstrated good accuracy in annual CH estimation compared to other CH data products when validated against GEDI and ALS datasets. Higher CH values are found in the northern and western parts of the African dense forest region, including Gabon, Cameroon, Equatorial Guinea, and the northern regions of the Republic of the Congo, where CH exceeds 40 m (Figure 5a). In these regions, our CH values are larger than in the Potapov and Paul CH maps. In contrast, the central Congo peat swamp forests and the riparian forests along the Congo River and its tributaries exhibited lower canopy height. This pattern aligned closely with the Lang CH but generally showed significantly higher CH values compared to the Potapov and Paul CH maps. When evaluated against independent GEDI RH100 data, our CH model gave a lower MAE (MAE = 5.93 m, Bias = 1.40 m) than the Lang CH model (MAE = 6.44 m, Bias = 2.54 m), followed by the Potapov and Paul CH models Figure 5b. The Potapov and Paul CH maps exhibited large underestimation biases, especially in tall forests higher than 30 m (bias of −7.48 m and −7.43 m) (Figure 5c). On the other hand, our model tends to overestimate GEDI RH100 values below 10 m, but less than the Lang CH. Validation against the ALS CH data confirms the accuracy of our model, with a smaller MAE (4.54 m) and Bias (−1.54 m), as well as reduced overestimations for low height, compared to three other CH maps

TABLE 3 Summary of global and regional aboveground biomass (AGB) maps in the African dense forest region across different mapping years. The ESACCI AGB dataset includes data from 2010 to 2015–2021, with the most recent map from 2021 used in this study. Since the dense forests in Central Africa were masked out in the AGB map from **Bouvet et al. (2018)**, we excluded this map from our comparison. DRC: Democratic Republic of Congo.

Data source	Spatial resolution	Spatial coverage	Mapping year
Saatchi et al. (2011)	1 km	Tropical regions	2000s
Avitabile et al. (2016)	1 km	Pan-tropics	2000s
Baccini et al. (2012)	500 m	Pan-tropics	2007–2008
GlobBiomass (Santoro et al., 2018)	100 m	Global	2010
Bouvet et al. (2018)	25 m	Africa	2010
Xu et al. (2017)	100 m	DRC	2013–2016
NCEO (Rodriguez-Veiga and Balzter, 2021)	100 m	Africa	2017
Sagang et al. (2024)	100 m	Gabon	2020
ESA CCI AGB v5.01 (Santoro and Cartus, 2024)	100 m	Global	2021
GEDI L4B AGB v2.1 (Dubayah et al., 2023)	1 km	51.6° S to 51.6° N	2019–2023

(Figure 6). Furthermore, to demonstrate the feasibility of our modeling framework for generating consistent annual maps, we evaluated the performance of the annual CH maps (2019–2022) using independent GEDI footprints reserved for model testing, as well as ALS data collected in the DRC (see Section 2.3.4). The results show relatively stable model performance across years (GEDI: MAE = 5.45–6.81 m; ALS: MAE = 4.46–4.74 m) (Supplementary Figure S9, S10).

The distribution of the differences between predicted and validation GEDI/ALS CH by 5-m intervals from 0 to 60 m, shows a shift from positive values (overestimations) at low CH to negative values at high CH levels (underestimations) (Figures 6a–d; Supplementary Figure S11). The presented CH data showed smaller differences to reference CH within tall forests (>30 m), with less saturation effects than Pauls and Potapov, but overestimations below 20 m. When compared to the Lang product, our CH data demonstrated smaller estimation errors for both short forests (<15 m) and tall forests (>30 m), with smaller bias across all ranges of the CH distribution (Figure 6d; Supplementary Figure S11d). Similar to the results shown in Figure 5, Potapov and Pauls give a better consistency with GEDI RH100 for forests under 25 m, but the comparison with ALS CH data did not demonstrate similar advantages. In contrast, our CH model showed an improved match with ALS CH values (Supplementary Figure S11).

Comparison of CH models with reference data from four selected ALS campaigns is shown in Figure 7. Due to their higher resolution, the ALS maps presented finer spatial details than what can be modelled from space (Figure 7a). While our CH map showed good consistency with the ALS CH map across varying canopy structures, some finer spatial details were smoothed (Figure 7b). The Lang model also captures spatial patterns, but with less sharpness and underestimations for higher CH values (Figure 7c). In contrast, most of the observed patterns in the reference data were absent in Potapov and Pauls (Figures 7d,e). Regarding CH variation along the ALS strips, both our CH map and Lang presented comparable values, yet our map gave a slightly better match in over tall forests (Figure 7f). We also compared our map with two recent ALS CH maps from 2023, and found good performances compared to other products (Supplementary Figure S12).

3.2 Validation and comparison of above ground biomass model

3.2.1 Validation with reference plot and LiDAR data

The AGB1 map shown in Figure 8 led to a MAE of 81.88 Mg/ha and a bias of 3.19 Mg/ha, following our 80%–20% cross validation procedure (Supplementary Figure S14). The AGB maps generated from variants of the AGB1 model showed slightly higher MAE and tended to saturate above 400 Mg/ha. The AGB2 map had the best performances but by a small margin, with a MAE of 79.65 Mg/ha. In particular, AGB2 improved the underestimation against validation data from DRC compared to AGB1. The variant of the AGB2 model calibrated only with ALS data from AfriSAR LVIS had no better performance than the AGB1 model (Supplementary Figures S15,S16) possibly because of inconsistency between WD used to calculate AGB from ALS by Armston et al. (2020) and our gridded WD dataset used for calibration and mapping. Results for the other AGB maps (Figures 8c–k) showed lower fit statistics and predictive performances (Supplementary Table S3; Supplementary Figure S14).

3.2.2 Comparisons of our biomass map with other satellite products

The AGB1 and AGB2 maps demonstrated overall better or comparable performance when compared to other published AGB maps (Table 3) when compared to independent field data used (Figures 8c–k). The AGB2 map exhibited the lowest errors (R^2 = 0.40, MAE = 79.65 Mg/ha, Bias = 6.47 Mg/ha). The ESA CCI AGB (Figure 8d, Bias = 13.47 Mg/ha) and Avitabile maps also had a small bias (Figure 8j, Bias = 1.00 Mg/ha) but exhibited low R^2 and large RMSE and MAE values; R^2 is important here because a very low R^2 indicates that the spatial distribution is poorly reproduced, making the map unreliable. The regional Sagang et al. AGB map over Gabon demonstrated good agreement with reference field plots and LVIS AGB (Figure 8e). The regional Xu map over DRC, which

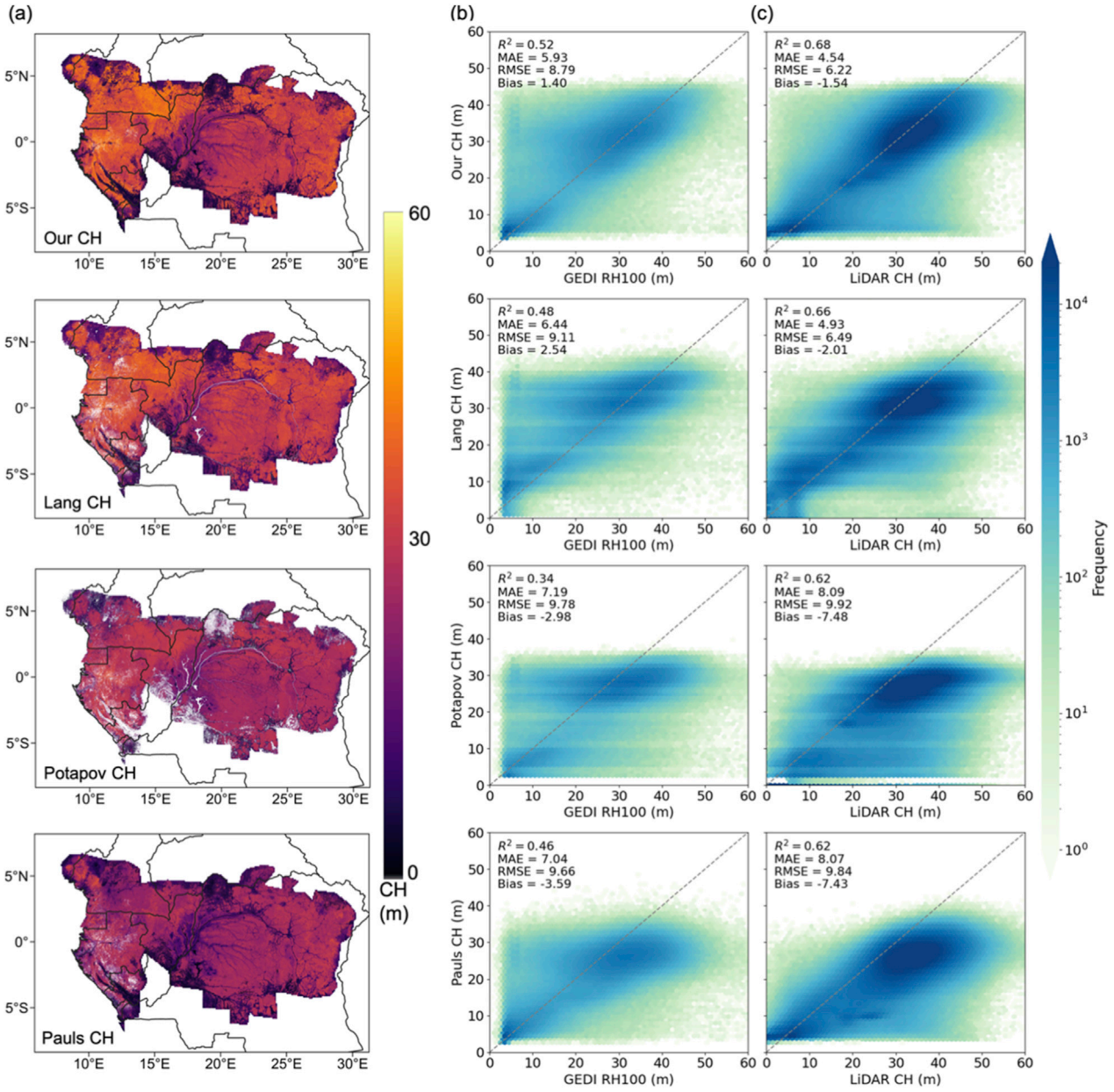

FIGURE 5
Visual and quantitative comparison of canopy height (CH) from this study and the global Lang, Potapov and Pauls products to the independent GEDI and airborne LiDAR CH data in the African dense forest region. **(a)** Visual maps of CH data from this study, Lang, Potapov and Pauls products. **(b,c)** Comparison of accuracy of estimated CH from this study, Lang, Potapov and Pauls products and measured CH from the independent GEDI **(b)** and airborne LiDAR **(c)** data.

utilized local ALS mean CH and more field data than us, demonstrated higher accuracy than our maps, with R^2 = 0.52, MAE = 67.49 Mg/ha, Bias = 4.42 Mg/ha in Xu et al. (2017).

The AGB2 map displayed higher AGB values in the DRC compared to AGB1, and showed more consistent spatial distributions with ESA CCI, NCEO Africa, and Xu maps (Figures 9a–k). We can also see in Figure 8 that the NCEO, GlobBiomass, and Saatchi maps (Figures 9f,h,k) do not exhibit clear spatial patterns, while the GEDI L4B map is too sparse to provide sufficient detail and shows lower values everywhere (Figure 9c). We identified similar spatial large-scale gradients between AGB1, AGB2, Avitabile, and ESA CCI, with high AGB in western Africa and low values in the central region over the Cuvette Centrale wetland. The NCEO map showed rather uniform high values across the Congo Basin. Comparing the differences between AGB1 and other products (Supplementary Figure S17), the GEDI AGB map exhibited considerable underestimation across all regions. Underestimated values were also found in earlier products from GlobBiomass, Baccini (in Western Africa), and Saatchi. We found that AGB1 had lower mean values in the DRC when compared to ESACCI, NCEO, and Xu. In contrast, AGB2 was closer to those maps in DRC (Supplementary Figure S18),

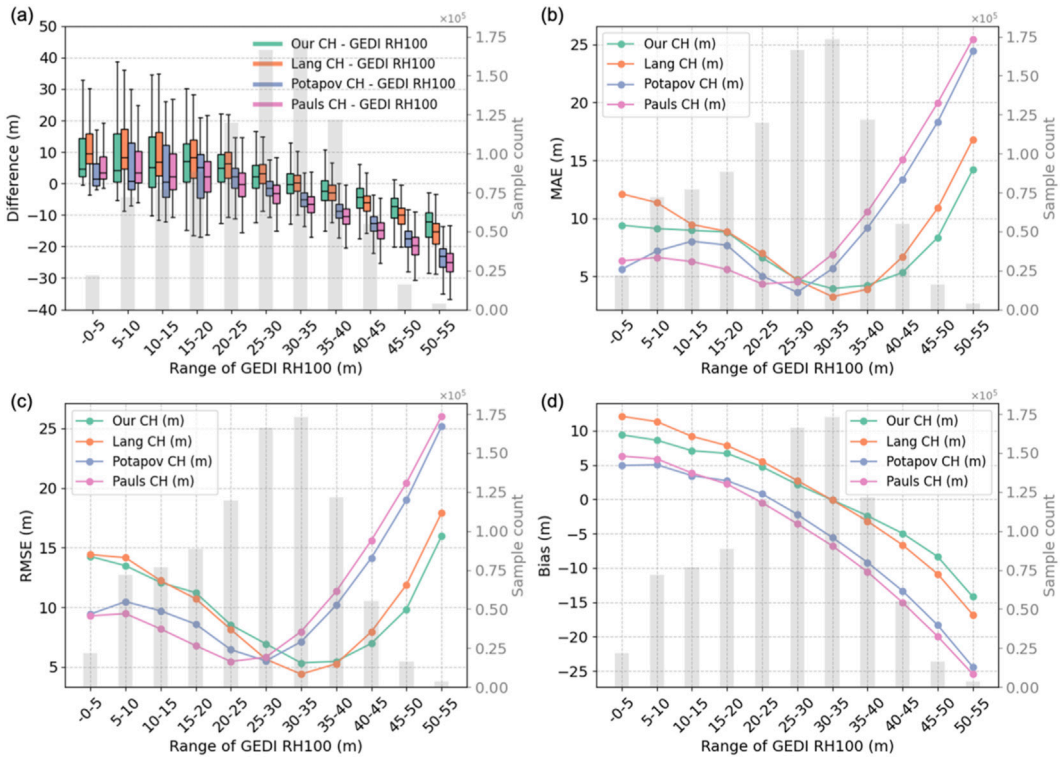

FIGURE 6
Distribution of differences between modeled CH and GEDI RH100 validation data in 5-m intervals from 0 to 60 m. The estimated CH includes four different data products: our CH (this study), and the global Lang, Potapov and Pauls CH products. **(a)** Difference between the four different CH data products and GEDI RH100. **(b–d)** Variations in estimation errors compared to GEDI RH100 validation data: **(b)** MAE, **(c)** RMSE, and **(d)** Bias, defined as modeled minus observed. All two comparisons in Figure 6a showed significant differences (P-value <0.05) based on the Kruskal–Wallis and Dunn's tests.

consistent with validation results in Figure 8. The spatial distributions of AGB1 and AGB2 for 2020, 2021, and 2022 are presented in Supplementary Figure S19 and are similar to those from the year 2019 (except for lower AGB over degraded and deforested pixels).

3.3 Biomass estimated using machine-learning for allometry

In the AGB3 and AGB4 models (Supplementary Figure S20) the residuals of the allometric AGB1 and AGB2 models were fitted using a XGBoost model. This XGBoost model explained 49% and 47% of the variance of the residuals, with CH input features accounting for 42% and 45% of the RE variance (Figure 10). WD explained 19.34% of the variance of the residuals of the AGB1 model, while CH metrics explained more variance of the residuals of the AGB2 model (Figures 10b,e). Additionally, CH metrics were more important in explaining the residuals of AGB1 than AGB2. Although these hybrid models achieved lower errors and bias values, they underestimated the residuals of high AGB field plots (absolute value >100 Mg/ha). The maps of residuals can further be used to understand the mapping differences of AGB3 and AGB4 vs. AGB1 and AGB2. The residuals of the AGB3 model show negative values in the DRC. The residuals of the AGB4 model show negative values in the central-northern region (Figures 10c,f). Furthermore, based on the residual model, we derived the spatial distribution of SHAP values for residual estimation in the AGB3 model (Supplementary Figure S21). Consistent with the results shown in Figure 10, WD, soil pH, and canopy height variance exhibited strong influence on biomass estimation. The AGB5 map generated directly using a XGBoost model for allometry is shown in Supplementary Figure S22. Overall, we found that AGB maps generated with machine learning models were prone to overfitting, particularly AGB5. Although they could reach a low MAE, their overall mapping performance remains limited due to biases at both low and high values compared to the more robust AGB1 and AGB2 (Supplementary Text 4). Further, all the maps derived using machine learning models tend to show spurious spatial patterns at small scale, reflecting the coarse resolution of their input features. For these two reasons, we do not recommend using these models for mapping AGB, until more realistic high resolution input data become available in the future.

3.4 Tracking biomass spatial patterns in forest concessions

The comparison of our AGB maps showed good consistency with concession data, that is AGB-P (Figures 11a,b,d,f; Supplementary Figures S23–S25). AGB2 better captured the spatial variation at 1 km of AGB-P than AGB1, as indicated by a

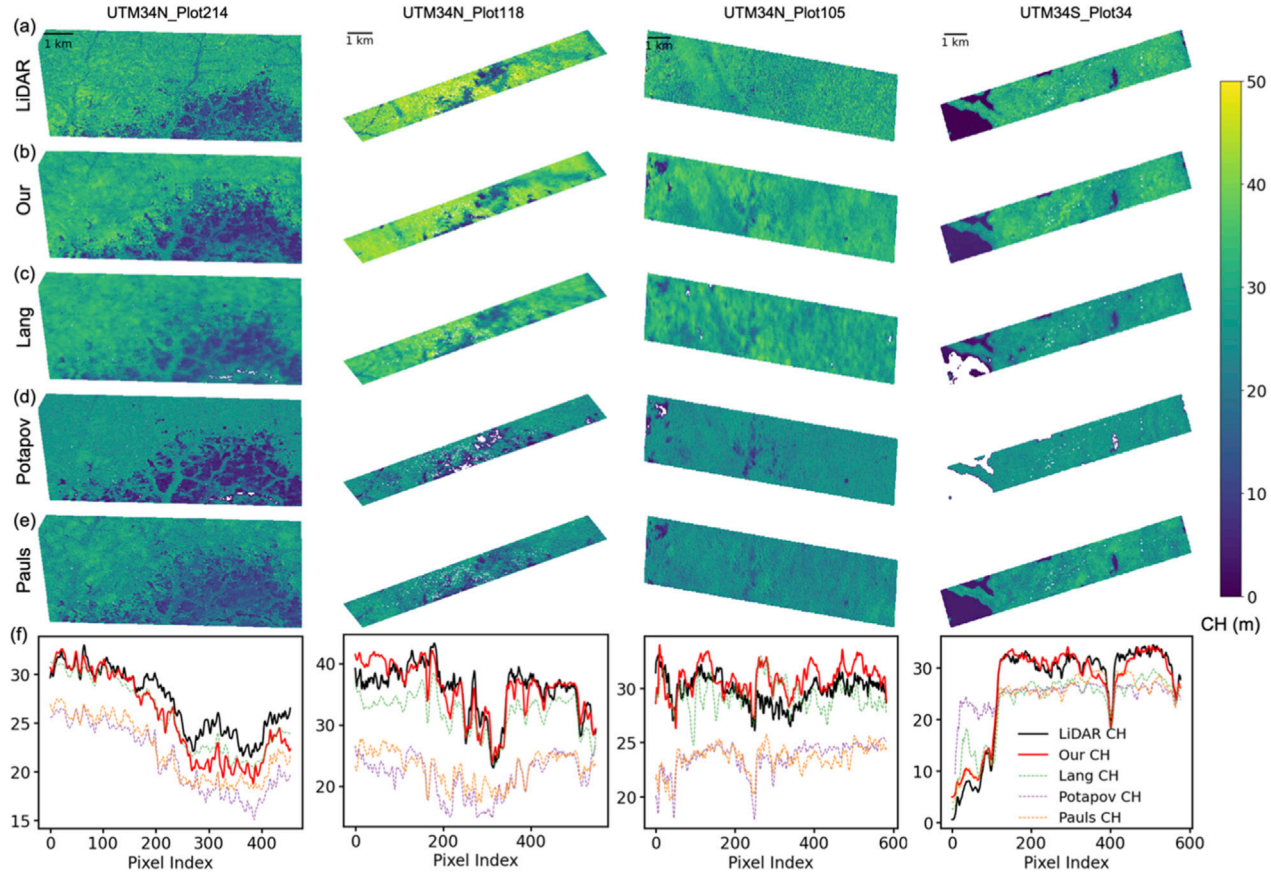

FIGURE 7
Comparison of the spatial distribution of the airborne LiDAR (ALS) CH map with our estimated CH and several global CH products from four different sampling plots: Plot214 (Lon: 22.180°~ 22.264°; Lat: 0.595°~0.646°), Plot118 (Lon: 18.824°~ 18.723°; Lat: 3.634°~3.699°), Plot105 (Lon: 18.867°~ 18.974°; Lat: 2.957°~2.973°), and Plot34 (Lon: 23.052°~ 23.158°; Lat: −3.184°~-3.139°). **(a–e)** Maps of CH map from **(a)** airborne LiDAR CH, **(b)** Our CH, **(c)** Lang CH, **(d)** Potapov CH, and **(e)** Pauls CH. **(f)** Comparison of changes in mean CH across the horizontal level over the Plot214, Plot118, Plot105, and Plot34. UTM34N refers to the Universal Transverse Mercator (UTM) Zone 34N, covering a region in the Northern Hemisphere with a longitudinal range of 18°E to 24°E.

higher R^2 value of 0.24. All forests in the AGB-P dataset have been harvested in the past, and either they experienced regrowth before our analysis period or they experienced a new disturbance. Regrowing forests were defined as those 1 km pixels that did not experience any disturbance event in Vancutsem et al. (2021) between the year of the inventory and our analysis period. Over these regrowing forests, the AGB difference between our maps and Ploton et al. (2020) exhibits a positive correlation with the time since forest regrowth (Figure 11c, Supplementary Text 5). On the other hand, for the forests that experienced at least one disturbance between the year of the field inventory and our analysis period, no notable biomass increase was observed, consistent with the fact that degradation has limited biomass regrowth (Figure 11e). During the lag period (Δt) between the year of our maps and the year of AGB-P data collection, AGB values have changed over time, with gains from forest regrowth and losses from degradation.

In the AGB-P areas that experienced forest regrowth since their sampling year, we found that the AGB1–5 maps all have higher mean AGB values than AGB-P which is consistent with regrowth gains of biomass since AGB-P data were collected (Supplementary Figures S26, S27). AGB2 had a R^2 of 0.36 (Figure 11). In the AGB-P areas that experienced degradation since the concession inventory date, R^2 equals 0.28. Interestingly, although the AGB3–5 maps had similar MAE of <80 Mg/ha, they showed a lower consistency with AGB-P, particularly at high AGB values (Supplementary Figure S25). We also compared the global and regional products with the AGB-P dataset, and found that our AGB2 dataset performed systematically better (Supplementary Figures S28–S30). Although the Sagang and Xu AGB maps showed smaller or comparable errors for Gabon and DRC respectively, they exhibited lower R^2 values with AGB-P. The Sagang, NCEO, GlobBiomass, Baccini and Saatchi AGB maps exhibited a saturation above 400 Mg/ha compared to AGB-P.

3.5 Tracking height and biomass changes

Our annual maps enable the tracking of changes in CH at 10 m and AGB at 30 m, providing key insights into forest disturbance and regrowth. Based on the CH change maps (Supplementary Figure S31), we observe clear spatial patterns of CH gains and losses from 2019 to 2022. Furthermore, the annual dataset allows us to identify the specific year in which forest disturbances occurred. For example, some forests

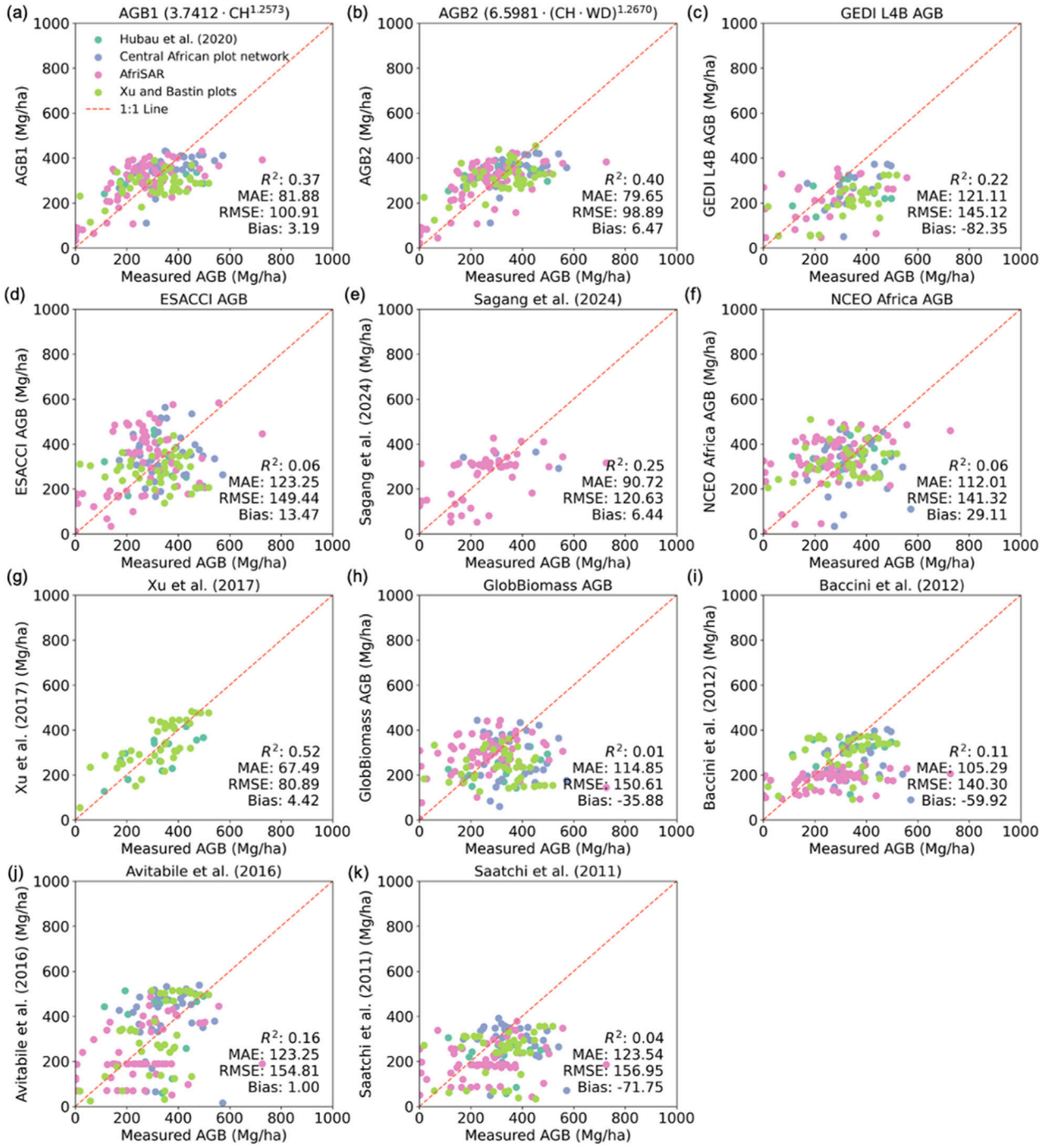

FIGURE 8
Comparison of field-measured aboveground biomass (AGB) with our maps and published AGB maps sampled at the field sites locations: **(a)** AGB1 (this study), **(b)** AGB2 (this study), **(c)** GEDI L4B AGB (Dubayah et al., 2023), **(d)** ESACCI AGB (Santoro and Cartus, 2024), **(e)** Sagang et al. (2024), **(f)** NCEO Africa AGB (Rodriguez-Veiga and Balzter, 2021), **(g)** Xu et al. (2017), **(h)** GlobBiomass (Santoro et al., 2018), **(i)** Baccini et al. (2012), **(j)** Avitabile et al. (2016), and **(k)** Saatchi et al. (2011). The performance of all AGB products was quantified using the 20% validation samples. The Sagang and Xu AGB maps cover only Gabon and the Democratic Republic of the Congo (DRC), respectively, leading to only partial overlap in the validation data. Additionally, the Xu AGB model was developed using some overlapped data from Xu and Bastin plots.

show gradual declines over multiple years (Supplementary Figures S31d,h,l), while others experienced abrupt losses in 2019 followed by stability (Supplementary Figure S31p). Our data combined with the TMF map can detect forest degradation, deforestation, and regrowth across a range of forest heights (Supplementary Text 6), particularly in young (short) regrowth and degraded forests below 10 m in 2019 (Figures 12c,e). Importantly, our results reveal substantial differences in CH and AGB across disturbed forest types. Mean AGB values in degraded (197.0 Mg/ha), deforested (146.6 Mg/ha), and regrowth (139.0 Mg/ha) areas were significantly lower than those in

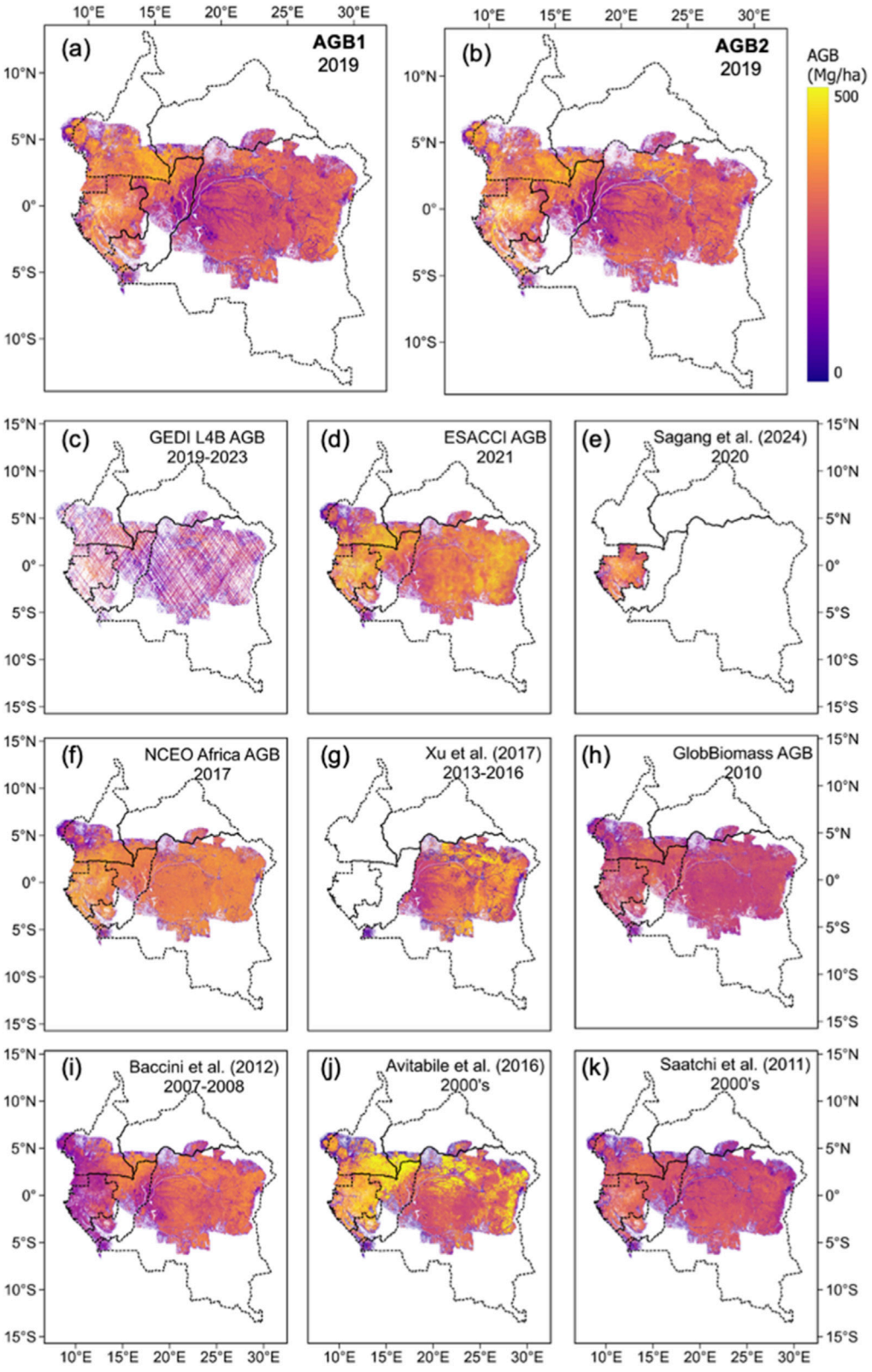

FIGURE 9
Comparison of the spatial distribution of aboveground biomass (Mg/ha) in the African dense forest region derived from multiple datasets: **(a)** this study AGB1 (30 m), **(b)** this study AGB2 (30 m), **(c)** GEDI L4B AGB (1 km), **(d)** ESACCI AGB (100 m), **(e)** Sagang (100 m), **(f)** NCEO Africa AGB (100 m), **(g)** Xu (100 m), **(h)** GlobBiomass (100 m), **(i)** Baccini (500 m), **(j)** Avitabile (1 km), and **(k)** Saatchi (1 km). AGB1 and AGB2 maps were generated using the canopy

(*Continued*)

FIGURE 9 (Continued)
height maps from this study and the best parametric models for allometric equations defined by Equation 2 and Equation 3, respectively. The approximate year of AGB mapping is indicated in the top-right corner of each panel with the reference name. All AGB maps were masked to align with our mapping region for the African dense forests, with non-forest pixels excluded.

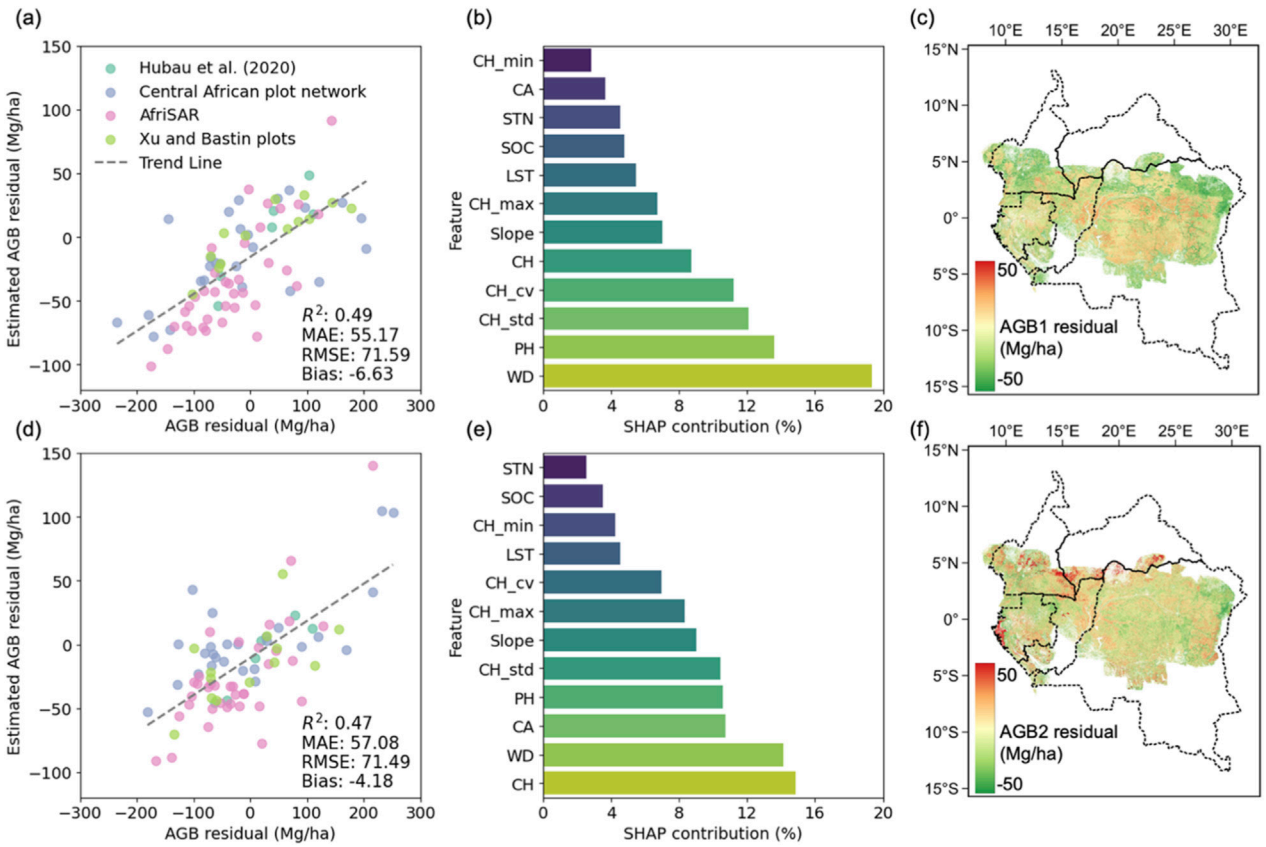

FIGURE 10
Evaluation of residuals from allometric AGB1 and AGB2 modeled by XGBoost models. **(a,d)** Relationship between measured (x-axis) and estimated AGB residuals for AGB1 and AGB2. **(b,e)** Contribution of each input variable to the estimated residuals of AGB1 and AGB2 based on the SHAP method. **(c,f)** Maps of the residuals from AGB1 and AGB2 models, generated using XGBoost models trained with CH and ancillary data, with green indicating overestimations and red indicating underestimations compared to the original AGB1 and AGB2 biomass maps.

undisturbed forests (314.8 Mg/ha) (Figures 12a,b). The annual maps also differentiate CH and AGB changes associated with various disturbance types (Figures 12d,f), particularly in deforested areas, which exhibit substantial biomass losses in tall, old-growth stands, where mean CH and AGB losses reach 14.5 m and 251.2 Mg/ha, respectively, and both variables were initially high. This highlights the value of annual CH and AGB monitoring in distinguishing subtle forest carbon dynamics that may not be captured by conventional disturbance maps alone.

4 Discussion

We developed and validated 10-m CH and 30-m AGB maps across African dense forests, mainly lowland forests. Overall, our maps showed good agreement with large-scale, multi-source independent validation data, achieving good accuracies for CH (R^2 = 0.68, MAE = 4.54 m, Bias = −1.54 m) and AGB (R^2 = 0.40, MAE = 79.65 Mg/ha, Bias = 6.47 Mg/ha). Compared to existing forest height and biomass products, our African forest product uniquely integrates multiple capabilities by combining annual-scale mapping, CH estimation, and AGB quantification at 10–30 m resolution using deep learning models. First, our framework enables automated generation of annual CH and AGB maps from 2019 onward, offering improved temporal consistency and accuracy. Second, our CH model uses only six bands from Sentinel-1 and Sentinel-2, yet achieves high spatial detail and reduced saturation in tall forests, even when trained with relatively limited data. This is made possible by the deep learning architecture, the use of year-specific models, and the integration of

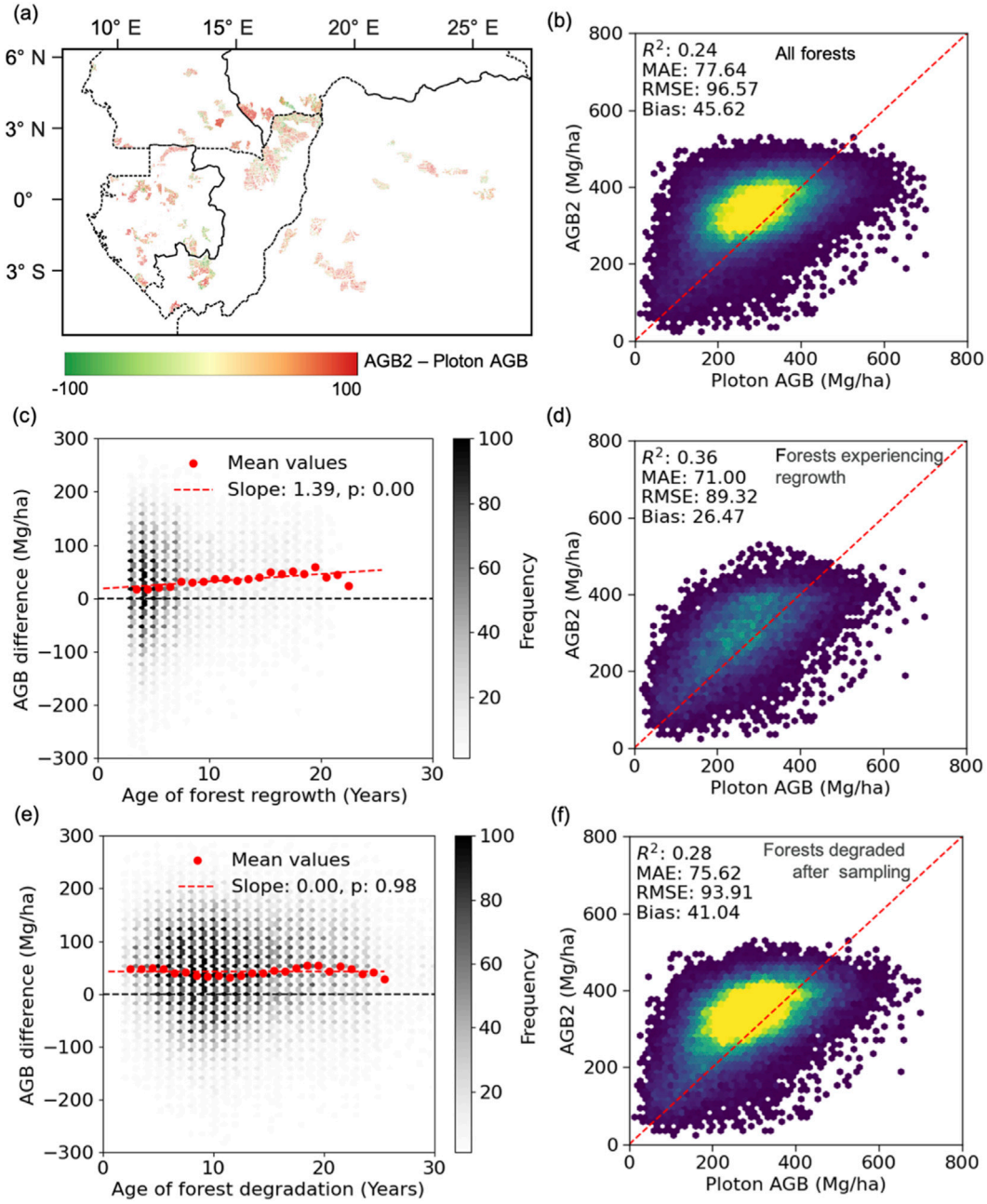

FIGURE 11
Evaluation of our best AGB map (AGB2) against Ploton AGB data (AGB-P) from forest concessions covering a large area. **(a)** Spatial differences between our AGB2 map aggregated at 1 km and the AGB-P map based on concession data collected years before our maps. **(b,d,f)** Relationships between our AGB maps and AGB-P across all forests **(b)**, forests experiencing regrowth **(d)**, and forests degraded after sampling by Ploton et al. (2020) **(f)**. The Ploton AGB data represent a 1-km resolution dataset aggregated from *in situ* forest management inventories (Ploton et al., 2020). Forest regrowth and degraded forest were classified based on the average age of forest regrowth and degradation within 1 km, using tropical moist forest (TMF) data from Vancutsem et al. (2021). **(c,e)** Relationship between the AGB difference and age of forest regrowth **(c)** and degraded forest **(e)**. The AGB difference was calculated as the AGB2 minus the Ploton AGB data. The average age of forest regrowth and degradation within 1 km was extracted from the TMF data.

Sentinel-1 SAR observations. Third, our AGB estimation strategy supports allometric, hybrid, and machine learning approaches, offering flexibility in estimating biomass and its associated uncertainties. Importantly, we incorporate a newly developed, spatially explicit wood density map to improve the accuracy of height-based biomass estimation. This factor has not been fully considered in previous large-scale biomass mapping efforts. As shown in Table 4, most previous CH or AGB products were limited to either one-time mapping or focused on a single variable, typically at a coarser resolution. In contrast, our model simultaneously supports high-resolution (10–30 m), annual-scale, and dual-variable (CH and AGB) estimation across African dense forests. By combining Sentinel-1/-2, GEDI, and wood density data, we provide a scalable and versatile monitoring system that enables

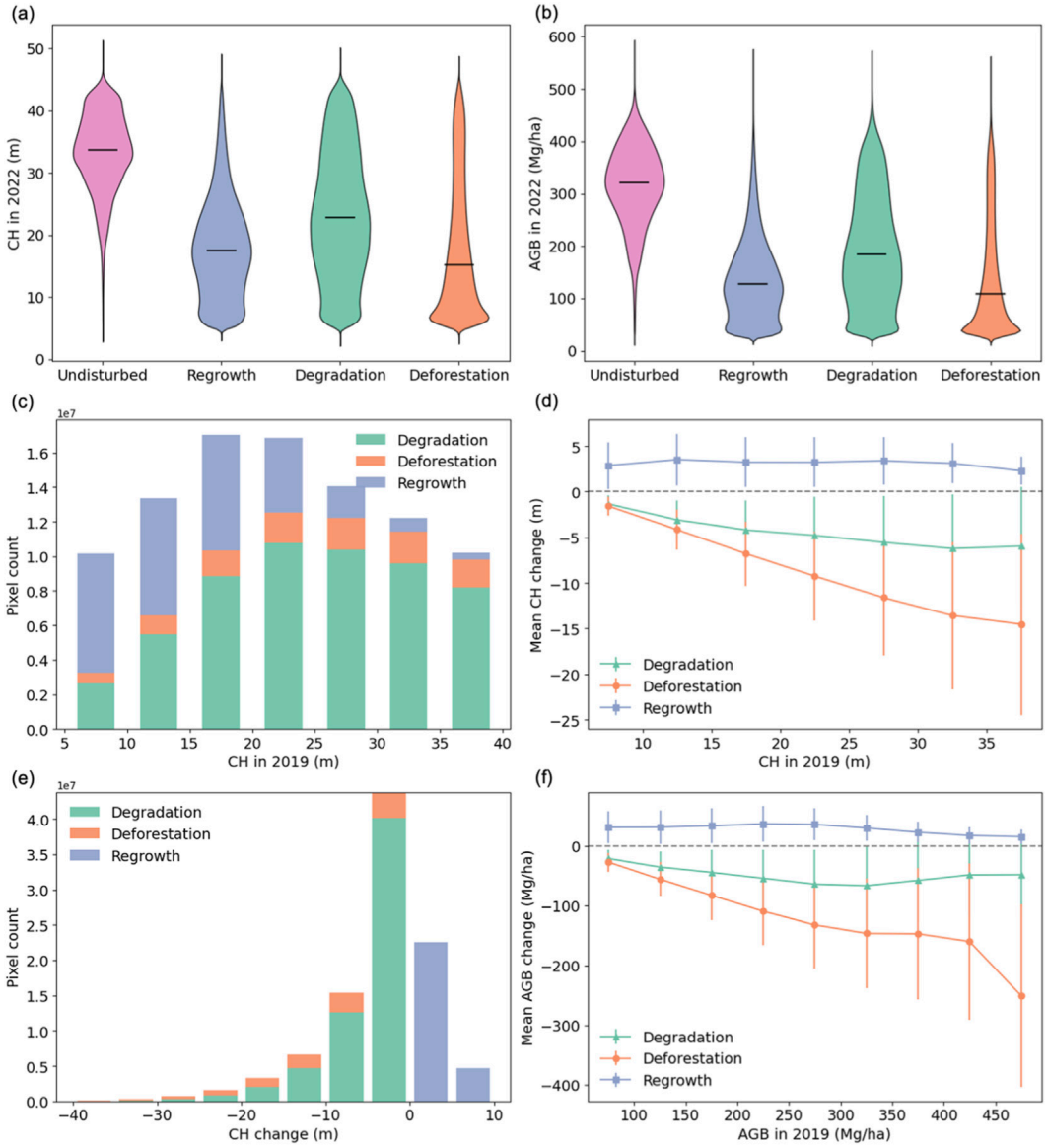

FIGURE 12
Canopy height (CH) and aboveground biomass (AGB) changes across different forest disturbance types. **(a,b)** Distributions of CH and AGB in 2022 across undisturbed, regrowth, degraded, and deforested forests. **(c)** Frequency distribution of regrowth, degradation, and deforestation events across varying CH values in 2019. **(d)** Mean CH changes (2019–2022) for regrowth, degradation, and deforestation across CH values in 2019. **(e)** Frequency distribution of regrowth, degradation, and deforestation events across varying CH change values from 2019 to 2022. **(f)** Mean AGB changes (2019–2022) for regrowth, degradation, and deforestation across AGB values in 2019. Disturbance categories (regrowth, degradation, and deforestation) were derived from the Tropical Moist Forest (TMF) dataset between 2019 and 2022.

the tracking of interannual changes in forest structure and carbon stocks, which was not previously achievable in large-scale forest products.

4.1 Canopy height mapping uncertainty

The choice of satellite imagery affects CH estimation due to variations in spatial resolution, spectral characteristics, and temporal availability. Sentinel-1/-2 images provide finer spatial details and thus they have higher potential in AGB estimation using the same modeling method, compared to Landsat imagery (Jha et al., 2021). This may lead to better performance in our CH than in Potapov CH and slightly better than in Lang CH. (Figures 5, 6; Supplementary Figure S11). Additionally, there is uncertainty regarding which Sentinel-2 wavebands should be used. Some studies have shown that employing all 10 bands can lead to more effective model training (Lang et al., 2023; Schwartz et al., 2024; Fayad et al., 2024). In this study, we excluded lower-resolution bands (e.g., 60 m) to reduce the training data size and better collocation with GEDI footprints. This choice is supported by Lang et al. (2019) and Schwartz et al. (2024) who demonstrated comparable performance using only four 10-m bands vs. all bands. Furthermore, while Sentinel-2 imagery has a nominal 10-m resolution for key bands,

TABLE 4 Summary of some commonly used or recently published canopy height and aboveground biomass maps in the African dense forest region. While GEDI collects data annually, its sparse spatial coverage limits its utility for annual mapping (Duncanson et al., 2022). Similarly, some biomass datasets with limited spatial and temporal coverage are not included in our comparison (see Table 3). S1/S2: Sentinel-1/-2; WV2/WV3: WorldView-2/-3; WD: wood density; CNN: convolutional neural network; OLS: ordinary least squares; BRT: bagged regression tree; SWR: stepwise regression; RF: random forest.

Study	Input data	Model	Resolution	Annual mapping	Canopy height	Biomass
This study	S1, S2, GEDI; WD	U-Net; Allometric	10 m 30 m	✓	✓	✓
Lang et al. (2023)	S2, GEDI	CNN	10 m		✓	
Potapov et al. (2021)	Landsat, GEDI	BRT	30 m		✓	
Pauls et al. (2024)	S1, S2, GEDI	U-Net	10 m		✓	
Tolan et al. (2024)	WV2, WV3, Quickbird II, ALS	DiNOv2	1 m		✓	
Santoro and Cartus (2024)	SAR C-band, L-band	Allometric, semi-empirical	100 m	✓		✓
Duncanson et al. (2022)	GEDI	Allometric, OLS	25 m		✓	✓
Xu et al. (2021)	SRTM, ALOS, Landsat, MODIS, QSCAT/VOD	Allometric RF	10 km	✓		✓
Baccini et al. (2017)	ICESat GLAS LiDAR, MODIS	Allometric SWR, RF	500 m	✓		✓
Yang et al. (2023)	L-VOD, four tropical/global biomass maps	Allometric	25 km	✓		✓

its effective resolution is often coarser due to the point spread function, adjacent effects, and incomplete atmospheric corrections. In heterogeneous landscapes, effective resolution may exceed 50 m (Choi et al., 2025). This leads to sub-pixel mixing and spectral contamination, reducing spatial detail in CH maps compared to ALS-derived CH maps of the same nominal resolution (Figure 7). In our study, Sentinel-1 help reduce saturation in tall forests, as shown by a regional experiment in Gabon (Supplementary Figure S3, S4) where the same U-Net model was trained with and without Sentinel-1 input. While this suggests that radar-derived texture provides useful contextual information for CH prediction, the observed improvement relative to Lang et al. (2023) may also result from the overall framework, which includes year-specific model training and a consistent input design. Nevertheless, previous studies have also reported the added value of combining Sentinel-1 and Sentinel-2 for CH estimation (Silveira et al., 2023; Schwartz et al., 2024).

Uncertainty of the GEDI target data also influences the accuracy and reliability of CH models. The CH model trained with the first-version GEDI product (R01) (Lang et al., 2023) was affected by misalignments resulting from geolocation uncertainty (e.g., >25 m). In contrast, our study and Pauls et al. (2024) used the updated GEDI R02 product for RH100, which features reduced geolocation errors, achieving a 1-sigma horizontal error within 10 m (Tang et al., 2023). It is likely that this improvement reduced biases, particularly in short forests where vegetation cover heterogeneity is larger and mixed effects from soil background are more pronounced. The selection of GEDI RH metrics (as RH100, RH98, RH95, . . .) affects CH model performance because different RH metrics vary greatly across different regions, leading to inconsistencies when applied to diverse target areas and validation datasets. Maximum RH metrics (R100 and RH98) should closely represent the actual top forest height but they are particularly sensitive to noise and uncertainties in waveform processing, especially for GEDI data with its large pulse width (Zhu et al., 2022). Thus, prior studies have primarily used GEDI RH98 rather than RH100 for CH model training (Lang et al., 2023; Li et al., 2023; Schwartz et al., 2023). Potapov et al. (2021) used GEDI RH95 as a reference, which matched well with ALS RH90 but could potentially underestimate dominant forest CH. Additionally, nearly all published models underestimated CH in tall forests (Figure 5) owing to saturation issues in optical satellite imagery and limitations in GEDI CH accuracy. All models also over-estimated short forests. The issue is close to what's known as "the dilution bias" in regression, and stems from the lack of information in model's covariates that would explain the variance in the dependent variable (here forest height). It is likely that using only RH95 and RH98 is not sufficient for accurate CH mapping in tropical forests, and including other RH metrics in the models may improve CH and AGB predictions (Xu et al., 2017; Sagang et al., 2024). In this study, RH100 was used, achieving better alignment than other CH metrics with both GEDI and ALS reference data. This selection required careful preprocessing to filter GEDI footprint points and enhance the quality of RH100 samples, as detailed in Section 2.2 and Pauls et al. (2024). Furthermore, despite the fact that the CH maps used for comparison used different RH metrics (RH98 or RH95), our CH RH100 model still demonstrated better performance against ALS heights: (1) The mean difference between RH95 used by Potapov et al. (2021) and our RH100 was about 3 m, significantly smaller than the estimation bias of 10 m observed in tall forests (Figure 6); (2) The RH98 map of Lang et al. underestimated CH in tall forests and overestimated it in short forests compared to our RH100 model. Adjusting RH98 to RH100 might reduce underestimation bias but could also introduce overestimation. Further validation with field-measured CH confirmed the advantages of our CH maps, which

exhibited smaller errors (Supplementary Figure S13) and greater spatial details compared than other CH products, especially in heterogeneous landscapes (Figure 7; Supplementary Figure S12).

4.2 Biomass mapping uncertainty

The performance of AGB maps strongly depends on the accuracy of CH maps. Current methods for AGB estimation primarily rely on the quantification of CH, an easier parameter to estimate across large areas. Our CH maps for African dense forests demonstrated higher accuracy than other available datasets, leading to more reliable AGB estimates. However, our model slightly overestimates CH in areas with trees shorter than 10 m. This bias is also present in the reference GEDI RH metrics, which may overestimate CH in low-stature forests depending on forest type and seasonal conditions (Dorado-Roda et al., 2021; Dhargay et al., 2022; Li et al., 2023). Despite this, our annual CH change maps effectively capture widespread degradation and regrowth dynamics, including those in low-stature forests (Figure 12). Moreover, most disturbances occur in medium-height forests, rather than in the shortest or tallest canopies. While the overestimation of CH in very short forests (<10 m) may have limited effect on disturbance detection and CH change estimates, it could influence the quantification of biomass accumulation during early regrowth stages. Further reducing CH estimation bias would likely benefit from training with ALS data or very high-resolution (<5 m) satellite imagery (Tolan et al., 2024; Wagner et al., 2025). While such data can improve per-pixel accuracy, they are often unavailable or prohibitively expensive across large tropical regions. Moreover, their limited spatial coverage and lack of regular updates make it difficult to train models that generalize well across time and space, and to validate annual predictions. As a result, these approaches are not yet feasible for generating spatially and temporally consistent annual CH maps at national or continental scales. Furthermore, our models were all developed based on top forest height (RH100) which primarily captures the structure of the upper canopy, but fails to account for variation in understory structure, adding uncertainty to AGB predictions (Duncanson et al., 2022). The combined use of multiple RH metrics (e.g., RH50 and RH75) along with other variables from the GEDI L2B product may thus improve AGB predictions (Duncanson et al., 2022; Rodda et al., 2024; Sagang et al., 2024; see also Supplementary Figures S32, S33). When different RH metrics are unavailable, extracting multiple CH data points (such as minimum and maximum values) should improve model performance (Figure 10; Supplementary Figure S22).

Mapping AGB from CH requires accurate allometric models. The CH-AGB relationship is nonlinear and influenced by forest structure, species composition, and environmental conditions. This complexity introduces uncertainties into the AGB modeling process. Most CH-AGB relationships can be described by a power-law relationship (Supplementary Table S1), but they vary across forest types (e.g., lowland vs. montane forests) and forest age. As forests mature, CH saturates while AGB continues to increase, making CH an incomplete predictor of forest biomass. Our AGB1 model using CH only was consistent with cross-validation field datasets and model aligned closely with previous allometric relationships derived from LVIS (Armston et al., 2020) and other studies (Simard et al., 2019; Stovall et al., 2021), suggesting its transferability across both field and ALS data. However, this allometric model underestimated biomass in the DRC forest (Figures 8, 9; Supplementary Figures S17,S18), primarily due to discrepancies between our CH estimates and those derived from ALS by Xu et al. (2017). We found that CH explains only 64.4% of the variability of biomass (Supplementary Figure S22). This finding is consistent with previous studies, highlighting the need to integrate other axes of AGB variation than forest height in AGB models, such as mean stand wood density and basal area, or covariates that may explain these variation axes (e.g., forest types) (Saatchi et al., 2011; Xu et al., 2017; Fatoyinbo et al., 2021). The AGB2 model based on CH and WD reduced the underestimation of high biomass in the DRC (Supplementary Figure S18). This highlights the necessity of integrating WD to improve large-scale biomass mapping. However, the limited spatial resolution of available WD maps (i.e., 1 km) still requires further refinement.

Furthermore, 10 m single-pixel CH data do not fully capture forest structural heterogeneity in a 30 m pixel defining biomass, making it necessary to account for CH variance within a 30 m pixel (Figure 10; Supplementary Figure S22). We tried to account for this heterogeneity within a 30 m biomass pixel by using machine learning for allometric models. Yet, the applicability of these models was hindered by the lack of training samples and high-resolution ancillary data. The limited number of field samples (N = 403) constrained the ability of XGBoost models to quantify residuals in AGB1 and AGB2, with only 47% and 49% of the residuals variance being explained. This limitation hinders our machine learning models from effectively capturing the residuals of AGB1 and AGB2 to achieve better mapping performance (Figure 10). Furthermore, the predictive capacity of machine learning models is significantly influenced by the range of valid samples. For instance, the lack of samples at low and high biomass values caused biases, with saturation at high values (Supplementary Figure S25), despite the overall reduction in model error (Supplementary Figure S22). Sparse or incomplete training data limited the allometric models' ability to capture the full spectrum of CH-AGB variability, particularly in underrepresented forest types or regions. While it is possible to combine multiple data sources to train allometric models, the differences between field plots and ALS-derived AGB still poses a challenge. Furthermore, mismatches in data resolution may have affected the quality of maps generated by machine learning models, potentially resulting in erroneous spatial details (Supplementary Figure S23). In addition to resolution mismatches, uncertainties in the input variables such as climate, soil, and forest type (Supplementary Table S2) could also propagate into the machine learning predictions. These ancillary datasets were not uniformly validated across the study region. Their spatial inaccuracies or thematic misclassifications may have introduced noise into model training and prediction (Supplementary Figure S21). For example, forest type maps may not capture fine-scale species composition or degradation status (Réjou-Méchain et al., 2021). Climate and soil layers may contain coarse-resolution artifacts that do not align with local canopy height variation (Hengl et al., 2021; Jimenez-Munoz et al., 2014). These sources of uncertainty likely contributed to the limited improvement of machine learning models compared to the simpler allometric approach based solely on CH.

Overall, compared to XGBoost models, the parametric allometric models produced more robust biomass maps, demonstrating a higher consistency with the independent large scale concession data of Ploton et al. (2020) (Figure 11).

4.3 Implications for future work

The GEDI data contains random geolocation errors, although the current version has been improved to meet the mission's 10-m, 1-sigma horizontal geolocation accuracy requirement (Tang et al., 2023). These geolocation errors result in a lack of fine spatial details, such as roads and crown gaps (Figure 7). Consequently, further efforts are needed to develop methods to address these issues. In addition, the Sentinel-2 data can be improved with corrected bidirectional reflectance (BRDF), which should be tested in further studies. One potentially efficient strategy would be to combine data from other sensors to enhance calibration and validation, such as integrating GEDI with ALS (Tang et al., 2023), ICESat-2 ATLAS (Liu et al., 2022), or TanDEM-X InSAR data (Qi et al., 2025) and L-band radar such as ALOS-PALSAR2 (Rosenqvist et al., 2014) which are more sensitive to deeper canopy structure than Sentinel-1. However, this approach will require careful consideration of system differences and ensuring sufficient spatial coverage. Another promising approach is to use ancillary data, such as leaf area index, vegetation indices and gross primary productivity, to identify the leaf-on seasons across the Central African forests (Liu et al., 2024) for better selecting GEDI footprints and mitigate RH variations that may occur during non-growing seasons when vegetation signals are weaker and more prone to geolocation misalignment.

Our AGB estimation inevitably exhibits some saturation, particularly in areas with very high biomass, reflecting limitations inherited from both CH models and the allometric relationships used to derive biomass. While we tested alternative approaches, including hybrid and machine learning models (e.g., XGBoost), these reduced numerical errors but introduced unrealistic spatial artifacts and relied on inputs not consistently available across years, making them unsuitable for annual mapping. In contrast, our selected method achieves a balance between accuracy, temporal consistency, and interpretability. The resulting AGB maps, with a relative RMSE of 32.9%, perform comparably to or better than recently developed biomass models and products (23.3%–76.1%) (Supplementary Table S4). More importantly, our framework enables the first annual, high-resolution (30 m) AGB maps for African tropical forests, addressing a long-standing gap in forest carbon monitoring and supporting operational applications across space and time.

Our biomass maps require further enhancement to better address uncertainties in model training and validation. To improve AGB modeling, in future work, we will train models using additional GEDI RH metrics than RH100. Achieving this will also demand significant time for model training. Another option is to develop region- and forest-type-specific AGB models based on CH and WD, which may better capture variability and reduce biases. For allometric models, continuing to test machine learning approaches could improve accuracy by integrating additional predictors like soil properties and environmental factors. Although allometric models should be robust enough to be applied to different forest types, the current study region is dominated by lowland dense forests. As such, the model was trained primarily on lowland conditions, and montane or dry forests were not sufficiently represented in the training data. Although our CH model performs consistently across different forest types (Supplementary Figure S34), performance slightly declines in montane regions, particularly above 2,000 m where our CH and GEDI RH100 correlations decrease (Supplementary Figure S35). This is likely due to a combination of factors, including increased terrain-induced geolocation errors, limited training samples at high elevations, and reduced accuracy of LiDAR-based CH retrievals in mountainous regions, where identifying reliable ground returns is more difficult (Liu et al., 2021; Lang et al., 2019; Dhargay et al., 2022). Consequently, AGB retrievals in these regions may be less reliable. Interestingly, our results still show comparable mean AGB values between lowland (elevation ≤800 m) and montane forests, consistent with the high carbon densities reported by Cuni-Sanchez et al. (2021) in montane forests. However, to improve the robustness of CH and AGB estimates in underrepresented forest types, especially montane forests, we plan to expand future model training to broader regions with enhanced ground reference data.

Model validation should fully account for the impact of field sampling and differences in mapping time. Currently, most available plot inventories and ALS data were collected over 10 years ago (Table 1) which degrades the match between field-observed and satellite-retrieved biomass. Although we mitigate this issue by applying recent forest masks, this significantly reduced data availability. Moreover, height and biomass in the tropics may change rapidly due to forest deforestation and degradation (Figure 12; Supplementary Figure S31), contributing to the differences between our maps and inventories (Figure 11, Supplementary Figure S25-S27). Therefore, it is important to identify if each field site has experienced no disturbance, or a disturbance followed by regrowth or degradation which can be done using historical disturbance datasets such as Vancutsem et al. (2021). This approach can further be combined with growth models to predict changes in forest biomass (Heinrich et al., 2023) between the year of inventory and the recent period analyzed by satellite data. Another option would be to use a longer time series of remote sensing data such as Landsat images, to infer CH and AGB with deep learning modes over the period covered by inventories.

5 Conclusion

This study presents a deep learning framework for mapping annual CH, successfully deriving AGB maps in African dense forests through allometric and machine learning methods. By integrating Sentinel-1/-2, GEDI data, and extensive reference datasets, the proposed methodology enhanced the estimation accuracy of CH (Bias = 1.40 m) and AGB (Bias = 6.47 Mg/ha) compared to most existing datasets. The high-resolution CH map demonstrates improved spatial detail and reduced bias compared to three global CH datasets, particularly in tall forests. The

optimized AGB maps outperformed commonly used datasets, showing good agreement with field observations. Our study developed an optimal allometric model for characterizing AGB variability from CH and WD, which exhibited high consistency across different data sources. We also provided residual maps for allometric AGB models as a reference, although the residual model can only be partially accepted. These findings emphasize the importance of further refining data integration and modeling techniques to enhance tropical forest carbon monitoring. Specifically, improved filtering approaches for GEDI footprints, based on the identification of leaf-on seasons, could reduce the impact of geolocation uncertainty. Additionally, integrating different RH metrics from GEDI and ALS is expected to enhance AGB estimation accuracy. It is also essential to mitigate the effects of forest regrowth and degradation on the alignment between remote sensing data and field plot measurements. Overall, this study presents the first version of the "FORest Multiple Source" CH and AGB maps for African dense forests (FORMS-Africa V1), which have the potential to track forest disturbances including degradation, deforestation, and regrowth through changes in CH and AGB. Future efforts will focus on enhancing the modeling framework and providing annual updates for the FORMS-Africa CH and AGB maps.

Data availability statement

The original contributions presented in the study are included in the article/Supplementary Material, further inquiries can be directed to the corresponding author.

Author contributions

LW: Writing – review and editing, Validation, Formal Analysis, Software, Writing – original draft, Visualization, Methodology, Conceptualization. PC: Visualization, Conceptualization, Resources, Funding acquisition, Project administration, Methodology, Supervision, Formal Analysis, Writing – original draft, Writing – review and editing. AdT: Methodology, Data curation, Conceptualization, Writing – review and editing, Validation, Investigation, Software. ES: Writing – review and editing, Software, Visualization, Methodology. FJF: Writing – review and editing, Data curation, Methodology. DP: Software, Writing – review and editing, Methodology. GB: Methodology, Software, Writing – review and editing. IF: Software, Writing – review and editing, Methodology. MS: Methodology, Software, Writing – review and editing. YX: Writing – review and editing, Methodology, Visualization. YS: Writing – review and editing, Methodology, Visualization. MR-M: Writing – review and editing. NB: Writing – review and editing. PT: Writing – review and editing. J-FB: Writing – review and editing, Investigation. JB: Investigation, Writing – review and editing. AVL: Writing – review and editing, Investigation. AP: Investigation, Writing – review and editing. BAI: Writing – review and editing, Investigation. D-MA: Writing – review and editing, Investigation. TdH: Writing – review and editing, Investigation. LBS: Writing – review and editing. LD: Writing – review and editing. YR: Writing – review and editing. TY: Writing – review and editing. CVO: Writing – review and editing. TB: Writing – review and editing. FF: Writing – review and editing. MP: Writing – review and editing. J-PW: Writing – review and editing. JC: Writing – review and editing. AC-S: Writing – review and editing. WH: Writing – review and editing. HV: Writing – review and editing. PB: Writing – review and editing. J-RM: Writing – review and editing, Investigation. CE: Writing – review and editing, Investigation. EK: Writing – review and editing. BS: Investigation, Writing – review and editing. ML: Investigation, Writing – review and editing. PP: Investigation, Writing – review and editing.

Funding

The authors declare that financial support was received for the research and/or publication of this article. We are grateful to the One Forest Vision initiative, funded by the French Ministry of Higher Education and Research and the French Ministry for Europe and Foreign Affairs, for their support. We acknowledge the open access to Sentinel-1/-2 imagery provided by the European Space Agency, GEDI datasets from NASA, and AfriSAR LVIS LiDAR datasets from the NASA AfriSAR Mission. Many thanks to all investigators and researchers for their significant efforts in collecting the field plot and ALS data used in this study. LW, DP, MP, F.F. and PC are supported by the One Forest Vision Initiative, a research project funded by the French Ministries of Research and Foreign Affairs to support the monitoring of forests in Central Africa. FJF acknowledges support from the European Research Council under the European Union's Horizon 2020 research and innovation program (Grant Agreement 101001905, FORWARD). We also thank CNES TOSCA program for supporting code development. JFB, AP and AVL benefited from the support of the CANOPI project (Grant/Award Number:0.0026.22) for ALS acquisitions, funded by the joined Exellence of Science call of FNRS and FWO in Belgium.

Conflict of interest

Authors AdT, ES, and IF were employed by Kayrros SAS.

The remaining authors declare that the research was conducted in the absence of any commercial or financial relationships that could be construed as a potential conflict of interest.

The author(s) declared that they were an editorial board member of Frontiers, at the time of submission. This had no impact on the peer review process and the final decision.

Generative AI statement

The authors declare that no Generative AI was used in the creation of this manuscript.

Any alternative text (alt text) provided alongside figures in this article has been generated by Frontiers with the support of artificial intelligence and reasonable efforts have been made to ensure

accuracy, including review by the authors wherever possible. If you identify any issues, please contact us.

Publisher's note

All claims expressed in this article are solely those of the authors and do not necessarily represent those of their affiliated organizations, or those of the publisher, the editors and the reviewers. Any product that may be evaluated in this article, or claim that may be made by its manufacturer, is not guaranteed or endorsed by the publisher.

Supplementary material

The Supplementary Material for this article can be found online at: https://www.frontiersin.org/articles/10.3389/frsen.2025.1724950/full#supplementary-material

References

Armston, J., Tang, H., Hancock, S., Marselis, S., Duncanson, L., Kellner, J., et al. (2020). *AfriSAR: Gridded Forest Biomass and Canopy Metrics Derived from LVIS, Gabon, 2016* (Version 1). ORNL Distributed Active Archive Center. doi:10.3334/ORNLDAAC/1775

Astola, H., Häme, T., Sirro, L., Molinier, M., and Kilpi, J. (2019). Comparison of Sentinel-2 and landsat 8 imagery for forest variable prediction in boreal region. *Remote Sens. Environ.* 223, 257–273. doi:10.1016/j.rse.2019.01.019

Avitabile, V., Herold, M., Heuvelink, G. B., Lewis, S. L., Phillips, O. L., Asner, G. P., et al. (2016). An integrated pan-tropical biomass map using multiple reference datasets. *Glob. Change Biology* 22, 1406–1420. doi:10.1111/gcb.13139

Baccini, A., Goetz, S. J., Walker, W. S., Laporte, N. T., Sun, M., Sulla-Menashe, D., et al. (2012). Estimated carbon dioxide emissions from tropical deforestation improved by carbon-density maps. *Nat. Clim. Change* 2, 182–185. doi:10.1038/nclimate1354

Baccini, A., Walker, W., Carvalho, L., Farina, M., Sulla-Menashe, D., and Houghton, R. A. (2017). Tropical forests are a net carbon source based on aboveground measurements of gain and loss. *Science* 358, 230–234. doi:10.1126/science.aam5962

Bossy, T., Ciais, P., Renaudineau, S., Wan, L., Ygorra, B., Adam, E., et al. (2025). State of the art in remote sensing monitoring of carbon dynamics in African tropical forests. *Front. Remote Sens.* 6, 1532280. doi:10.3389/frsen.2025.1532280

Bouvet, A., Mermoz, S., Le Toan, T., Villard, L., Mathieu, R., Naidoo, L., et al. (2018). An above-ground biomass map of African Savannahs and woodlands at 25 m resolution derived from ALOS PALSAR. *Remote Sensing Environment* 206, 156–173. doi:10.1016/j.rse.2017.12.030

Chave, J., Coomes, D., Jansen, S., Lewis, S. L., Swenson, N. G., and Zanne, A. E. (2009). Towards a worldwide wood economics spectrum. *Ecol. Letters* 12, 351–366. doi:10.1111/j.1461-0248.2009.01285.x

Chave, J., Réjou-Méchain, M., Búrquez, A., Chidumayo, E., Colgan, M. S., Delitti, W. B., et al. (2014). Improved allometric models to estimate the aboveground biomass of tropical trees. *Glob. Change Biology* 20, 3177–3190. doi:10.1111/gcb.12629

Chen, T., and Guestrin, C. (2016). "Xgboost: a scalable tree boosting system," in *Proceedings of the 22nd acm sigkdd international conference on knowledge discovery and data mining* (Association for Computing Machinery), 785–794. doi:10.1145/2939672.2939785

Choi, W., Ryu, Y., Kong, J., Jeong, S., and Lee, K. (2025). Evaluation of spatial and temporal variability in Sentinel-2 surface reflectance on a rice paddy landscape. *Agric. For. Meteorology* 363, 110401. doi:10.1016/j.agrformet.2025.110401

Ciais, P., Bombelli, A., Williams, M., Piao, S. L., Chave, J., Ryan, C. M., et al. (2011). The carbon balance of Africa: synthesis of recent research studies. *Philosophical Trans. R. Soc. A Math. Phys. Eng. Sci.* 369, 2038–2057. doi:10.1098/rsta.2010.0328

Crezee, B., Dargie, G. C., Ewango, C. E., Mitchard, E. T., Emba B, O., Kanyama T, J., et al. (2022). Mapping peat thickness and carbon stocks of the central Congo Basin using field data. *Nat. Geosci.* 15, 639–644. doi:10.1038/s41561-022-00966-7

Cuni-Sanchez, A., Sullivan, M. J. P., Platts, P. J., Lewis, S. L., Marchant, R., Imani, G., et al. (2021). High aboveground carbon stock of African tropical montane forests. *Nature* 596, 536–542. doi:10.1038/s41586-021-03728-4

Curtis, P. G., Slay, C. M., Harris, N. L., Tyukavina, A., and Hansen, M. C. (2018). Classifying drivers of global forest loss. *Science* 361, 1108–1111. doi:10.1126/science.aau3445

Dhargay, S., Lyell, C. S., Brown, T. P., Inbar, A., Sheridan, G. J., and Lane, P. N. J. (2022). Performance of GEDI space-borne LiDAR for quantifying structural variation in the temperate forests of south-eastern Australia. *Remote Sens.* 14, 3615. doi:10.3390/rs14153615

Dorado-Roda, I., Pascual, A., Godinho, S., Silva, C. A., Botequim, B., Rodríguez-Gonzálvez, P., et al. (2021). Assessing the accuracy of GEDI data for canopy height and aboveground biomass estimates in mediterranean forests. *Remote Sens.* 13, 2279. doi:10.3390/rs13122279

Dubayah, R., Blair, J. B., Goetz, S., Fatoyinbo, L., Hansen, M., Healey, S., et al. (2020a). The global ecosystem dynamics investigation: high-resolution laser ranging of the Earth's forests and topography. *Sci. Remote Sensing* 1, 100002. doi:10.1016/j.srs.2020.100002

Dubayah, R., Hofton, M., Blair, J., Armston, J., Tang, H., and Luthcke, S. (2020b). *GEDI L2A Elevation and Height Metrics Data Global Footprint Level V002* [Data set]. NASA Land Processes Distributed Active Archive Center. doi:10.5067/GEDI/GEDI02_A.002

Dubayah, R., Armston, J., Healey, S., Yang, Z., Patterson, P., Saarela, S., et al. (2023). *GEDI L4B Gridded Aboveground Biomass Density, Version 2.1* (Version 2.1). ORNL Distributed Active Archive Center. doi:10.3334/ORNLDAAC/2299

Duncanson, L., Armston, J., Disney, M., Avitabile, V., Barbier, N., Calders, K., et al. (2019). The importance of consistent global forest aboveground biomass product validation. *Surv. Geophysics* 40, 979–999. doi:10.1007/s10712-019-09538-8

Duncanson, L., Kellner, J. R., Armston, J., Dubayah, R., Minor, D. M., Hancock, S., et al. (2022). Aboveground biomass density models for NASA's global ecosystem dynamics investigation (GEDI) lidar mission. *Remote Sens. Environ.* 270, 112845. doi:10.1016/j.rse.2021.112845

Duncanson, L., Hunka, N., Jucker, T., Armston, J., Harris, N., Fatoyinbo, L., et al. (2025). Spatial resolution for forest carbon maps. *Science* 387, 370–371. doi:10.1126/science.adt6811

Fan, L., Wigneron, J.-P., Ciais, P., Chave, J., Brandt, M., Fensholt, R., et al. (2019). Satellite-observed pantropical carbon dynamics. *Nat. Plants* 5, 944–951. doi:10.1038/s41477-019-0478-9

Farr, T. G., Rosen, P. A., Caro, E., Crippen, R., Duren, R., Hensley, S., et al. (2007). The shuttle radar topography mission. *Rev. Geophysics* 45. doi:10.1029/2005rg000183

Fassnacht, F. E., Poblete-Olivares, J., Rivero, L., Lopatin, J., Ceballos-Comisso, A., and Galleguillos, M. (2021). Using Sentinel-2 and canopy height models to derive a landscape-level biomass map covering multiple vegetation types. *Int. J. Appl. Earth Observation Geoinformation* 94, 102236. doi:10.1016/j.jag.2020.102236

Fassnacht, F. E., White, J. C., Wulder, M. A., and Næsset, E. (2024). Remote sensing in forestry: current challenges, considerations and directions. *For. Int. J. For. Res.* 97, 11–37. doi:10.1093/forestry/cpad024

Fatoyinbo, T., Armston, J., Simard, M., Saatchi, S., Denbina, M., Lavalle, M., et al. (2021). The NASA AfriSAR campaign: airborne SAR and lidar measurements of tropical forest structure and biomass in support of current and future space missions. *Remote Sens. Environ.* 264, 112533. doi:10.1016/j.rse.2021.112533

Fayad, I., Ciais, P., Schwartz, M., Wigneron, J. P., Baghdadi, N., de Truchis, A., et al. (2024). Hy-TeC: a hybrid vision transformer model for high-resolution and large-scale mapping of canopy height. *Remote Sens. Environ.* 302, 113945. doi:10.1016/j.rse.2023.113945

Fischer, F. J., Chave, J., Zanne, A., Jucker, T., Fajardo, A., Fayolle, A., et al. (2025). *A global map of wood density*. bioRxiv, 2025.2008. 2025.671920.

Fogel, F., Perron, Y., Besic, N., Saint-André, L., Pellissier-Tanon, A., Schwartz, M., et al. (2025). "Open-canopy: towards very high resolution forest monitoring," in *Proceedings of the computer vision and pattern recognition conference*, 1395–1406.

Hansen, M. C., Potapov, P. V., Moore, R., Hancher, M., Turubanova, S. A., Tyukavina, A., et al. (2013). High-resolution global maps of 21st-century forest cover change. *Science* 342, 850–853. doi:10.1126/science.1244693

Heinrich, V. H., Vancutsem, C., Dalagnol, R., Rosan, T. M., Fawcett, D., Silva-Junior, C. H., et al. (2023). The carbon sink of secondary and degraded humid tropical forests. *Nature* 615, 436–442. doi:10.1038/s41586-022-05679-w

Hengl, T., Miller, M. A., Križan, J., Shepherd, K. D., Sila, A., Kilibarda, M., et al. (2021). African soil properties and nutrients mapped at 30 m spatial resolution using two-scale ensemble machine learning. *Sci. Reports* 11, 6130. doi:10.1038/s41598-021-85639-y

Hubau, W., Lewis, S. L., Phillips, O. L., Affum-Baffoe, K., Beeckman, H., Cuní-Sanchez, A., et al. (2020). Asynchronous carbon sink saturation in African and Amazonian tropical forests. *Nature* 579, 80–87. doi:10.1038/s41586-020-2035-0

Jha, N., Tripathi, N. K., Barbier, N., Virdis, S. G. P., Chanthorn, W., Viennois, G., et al. (2021). The real potential of current passive satellite data to map aboveground biomass in tropical forests. *Remote Sens. Ecol. Conservation* 7, 504–520. doi:10.1002/rse2.203

Jimenez-Munoz, J. C., Sobrino, J. A., Skoković, D., Mattar, C., and Cristobal, J. (2014). Land surface temperature retrieval methods from Landsat-8 thermal infrared sensor data. *IEEE Geoscience Remote Sensing Letters* 11, 1840–1843. doi:10.1109/lgrs.2014.2312032

Labriere, N., Tao, S., Chave, J., Scipal, K., Le Toan, T., Abernethy, K., et al. (2018). *In situ* reference datasets from the TropiSAR and AfriSAR campaigns in support of upcoming spaceborne biomass missions. *IEEE J. Sel. Top. Appl. Earth Observations Remote Sens.* 11, 3617–3627. doi:10.1109/jstars.2018.2851606

Lang, N., Schindler, K., and Wegner, J. D. (2019). Country-wide high-resolution vegetation height mapping with Sentinel-2. *Remote Sens. Environ.* 233, 111347. doi:10.1016/j.rse.2019.111347

Lang, N., Jetz, W., Schindler, K., and Wegner, J. D. (2023). A high-resolution canopy height model of the Earth. *Nat. Ecol. and Evol.* 7, 1778–1789. doi:10.1038/s41559-023-02206-6

Li, X., Wessels, K., Armston, J., Hancock, S., Mathieu, R., Main, R., et al. (2023). First validation of GEDI canopy heights in African savannas. *Remote Sens. Environ.* 285, 113402. doi:10.1016/j.rse.2022.113402

Liang, M., Duncanson, L., Silva, J. A., and Sedano, F. (2023). Quantifying aboveground biomass dynamics from charcoal degradation in Mozambique using GEDI lidar and landsat. *Remote Sens. Environ.* 284, 113367. doi:10.1016/j.rse.2022.113367

Liu, A., Cheng, X., and Chen, Z. (2021). Performance evaluation of GEDI and ICESat-2 laser altimeter data for terrain and canopy height retrievals. *Remote Sens. Environ.* 264, 112571. doi:10.1016/j.rse.2021.112571

Liu, X., Su, Y., Hu, T., Yang, Q., Liu, B., Deng, Y., et al. (2022). Neural network guided interpolation for mapping canopy height of China's forests by integrating GEDI and ICESat-2 data. *Remote Sens. Environ.* 269, 112844. doi:10.1016/j.rse.2021.112844

Liu, L., Ciais, P., Maignan, F., Zhang, Y., Viovy, N., Peaucelle, M., et al. (2024). Solar radiation triggers the bimodal leaf phenology of central African evergreen broadleaved forests. *J. Adv. Model. Earth Syst.* 16, e2023MS004014. doi:10.1029/2023ms004014

Lundberg, S. (2017). *A unified approach to interpreting model predictions*. arXiv preprint arXiv:1705.07874.

McRoberts, R. E., Næsset, E., Heikkinen, J., and Strimbu, V. (2024). Two-stage, model-assisted estimation using remotely sensed auxiliary data. *Remote Sens. Environ.* 307, 114125. doi:10.1016/j.rse.2024.114125

Moudrý, V., Gábor, L., Marselis, S., Pracná, P., Barták, V., Prošek, J., et al. (2024). Comparison of three global canopy height maps and their applicability to biodiversity modeling: Accuracy issues revealed. *Ecosphere* 15, e70026. doi:10.1002/ecs2.70026

Nelson, R., Oderwald, R., and Gregoire, T. G. (1997). Separating the ground and airborne laser sampling phases to estimate tropical forest basal area, volume, and biomass. *Remote Sens. Environ.* 60, 311–326. doi:10.1016/s0034-4257(96)00213-1

Neuenschwander, A., and Pitts, K. (2019). The ATL08 land and vegetation product for the ICESat-2 mission. *Remote Sensing Environment* 221, 247–259. doi:10.1016/j.rse.2018.11.005

Pan, Y., Birdsey, R. A., Phillips, O. L., Houghton, R. A., Fang, J., Kauppi, P. E., et al. (2024). The enduring world forest carbon sink. *Nature* 631, 563–569. doi:10.1038/s41586-024-07602-x

Pauls, J., Zimmer, M., Kelly, U. M., Schwartz, M., Saatchi, S., Ciais, P., et al. (2024). *Estimating canopy height at scale*. arXiv preprint arXiv:2406.01076.

Ploton, P., Mortier, F., Barbier, N., Cornu, G., Réjou-Méchain, M., Rossi, V., et al. (2020). A map of African humid tropical forest aboveground biomass derived from management inventories. *Sci. Data* 7, 221. doi:10.1038/s41597-020-0561-0

Potapov, P., Li, X., Hernandez-Serna, A., Tyukavina, A., Hansen, M. C., Kommareddy, A., et al. (2021). Mapping global forest canopy height through integration of GEDI and landsat data. *Remote Sens. Environ.* 253, 112165. doi:10.1016/j.rse.2020.112165

Potapov, P., Hansen, M. C., Pickens, A., Hernandez-Serna, A., Tyukavina, A., Turubanova, S., et al. (2022). The global 2000-2020 land cover and land use change dataset derived from the landsat archive: first results. *Front. Remote Sens.* 3, 856903. doi:10.3389/frsen.2022.856903

Pourshamsi, M., Xia, J., Yokoya, N., Garcia, M., Lavalle, M., Pottier, E., et al. (2021). Tropical forest canopy height estimation from combined polarimetric SAR and LiDAR using machine-learning. *ISPRS J. Photogrammetry Remote Sens.* 172, 79–94. doi:10.1016/j.isprsjprs.2020.11.008

Qi, W., and Dubayah, R. O. (2016). Combining Tandem-X InSAR and simulated GEDI lidar observations for forest structure mapping. *Remote Sensing Environ.* 187, 253–266. doi:10.1016/j.rse.2016.10.018

Qi, W., Armston, J., Choi, C., Stovall, A., Saarela, S., Pardini, M., et al. (2025). Mapping large-scale pantropical forest canopy height by integrating GEDI lidar and TanDEM-X InSAR data. *Remote Sens. Environ.* 318, 114534. doi:10.1016/j.rse.2024.114534

Raven, P. H., Gereau, R. E., Phillipson, P. B., Chatelain, C., Jenkins, C. N., and Ulloa Ulloa, C. (2020). The distribution of biodiversity richness in the tropics. *Sci. Adv.* 6, eabc6228. doi:10.1126/sciadv.abc6228

Réjou-Méchain, M., Barbier, N., Couteron, P., Ploton, P., Vincent, G., Herold, M., et al. (2019). Upscaling forest biomass from field to satellite measurements: sources of errors and ways to reduce them. *Surv. Geophys.* 40, 881–911. doi:10.1007/s10712-019-09532-0

Réjou-Méchain, M., Mortier, F., Bastin, J.-F., Cornu, G., Barbier, N., Bayol, N., et al. (2021). Unveiling African rainforest composition and vulnerability to global change. *Nature* 593, 90–94. doi:10.1038/s41586-021-03483-6

Rodda, S. R., Fararoda, R., Gopalakrishnan, R., Jha, N., Réjou-Méchain, M., Couteron, P., et al. (2024). LiDAR-based reference aboveground biomass maps for tropical forests of south Asia and Central Africa. *Sci. Data* 11, 334. doi:10.1038/s41597-024-03162-x

Rodriguez-Veiga, P., and Balzter, H. (2021). *Africa aboveground biomass map for 2017*. UK: University of Leicester, 10.

Ronneberger, O., Fischer, P., and Brox, T. (2015). "U-net: convolutional networks for biomedical image segmentation," in Medical image computing and computer-assisted intervention–MICCAI 2015: 18th international conference, Munich, Germany, October 5-9, 2015 (Springer), 234–241.

Rosenqvist, A., Shimada, M., Suzuki, S., Ohgushi, F., Tadono, T., Watanabe, M., et al. (2014). Operational performance of the ALOS global systematic acquisition strategy and observation plans for ALOS-2 PALSAR-2. *Remote Sens. Environ.* 155, 3–12. doi:10.1016/j.rse.2014.04.011

Saatchi, S. S., Harris, N. L., Brown, S., Lefsky, M., Mitchard, E. T., Salas, W., et al. (2011). Benchmark map of forest carbon stocks in tropical regions across three continents. *Proc. National Academy Sciences* 108, 9899–9904. doi:10.1073/pnas.1019576108

Saatchi, S., Chave, J., Labriere, N., Barbier, N., Réjou-Méchain, M., Ferraz, A., et al. (2019). *AfriSAR: Aboveground Biomass for Lope, Mabounie, Mondah, and Rabi Sites, Gabon* (Version 1). ORNL Distributed Active Archive Center. doi:10.3334/ORNLDAAC/1681

Sagang, L. B. T., Favrichon, S., Dalagnol, R., Ordway, E. M., Medjibe, V., Manfoumbi, F., et al. (2024). Unveiling spatial variations of high forest live biomass carbon stocks of Gabon using advanced remote sensing techniques. *Environ. Res. Lett.* 19, 074038. doi:10.1088/1748-9326/ad5572

Santoro, M., and Cartus, O. (2024). *ESA biomass climate change initiative (Biomass_cci): global datasets of forest above-ground biomass for the years 2010, 2015, 2016, 2017, 2018, 2019, 2020 and 2021, v5.01., NERC EDS centre for environmental data analysis.*

Santoro, M., Cartus, O., Mermoz, S., Bouvet, A., Le Toan, T., Carvalhais, N., et al. (2018). *GlobBiomass global above-ground biomass and growing stock volume datasets*. Technical Report.

Schwartz, M., Ciais, P., De Truchis, A., Chave, J., Ottlé, C., Vega, C., et al. (2023). FORMS: forest multiple source height, wood volume, and biomass maps in France at 10 to 30 m resolution based on Sentinel-1, Sentinel-2, and global ecosystem dynamics investigation (GEDI) data with a deep learning approach. *Earth Syst. Sci. Data* 15, 4927–4945. doi:10.5194/essd-15-4927-2023

Schwartz, M., Ciais, P., Ottlé, C., De Truchis, A., Vega, C., Fayad, I., et al. (2024). High-resolution canopy height map in the Landes forest (France) based on GEDI, Sentinel-1, and Sentinel-2 data with a deep learning approach. *Int. J. Appl. Earth Observation Geoinformation* 128, 103711. doi:10.1016/j.jag.2024.103711

Silveira, E. M. O., Radeloff, V. C., Martinuzzi, S., Martinez Pastur, G. J., Bono, J., Politi, N., et al. (2023). Nationwide native forest structure maps for Argentina based on forest inventory data, SAR Sentinel-1 and vegetation metrics from Sentinel-2 imagery. *Remote Sens. Environ.* 285, 113391. doi:10.1016/j.rse.2022.113391

Simard, M., Pinto, N., Fisher, J. B., and Baccini, A. (2011). Mapping forest canopy height globally with spaceborne lidar. *J. Geophys. Res. Biogeosciences* 116, G04021. doi:10.1029/2011jg001708

Simard, M., Fatoyinbo, L., Smetanka, C., Rivera-Monroy, V. H., Castañeda-Moya, E., Thomas, N., et al. (2019). Mangrove canopy height globally related to precipitation, temperature and cyclone frequency. *Nat. Geosci.* 12, 40–45. doi:10.1038/s41561-018-0279-1

Small, D. (2011). Flattening gamma: radiometric terrain correction for SAR imagery. *IEEE Trans. Geoscience Remote Sens.* 49, 3081–3093. doi:10.1109/tgrs.2011.2120616

Stovall, A. E. L., Fatoyinbo, T., Thomas, N. M., Armston, J., Ebanega, M. O., Simard, M., et al. (2021). Comprehensive comparison of airborne and spaceborne SAR and LiDAR estimates of forest structure in the tallest mangrove forest on earth. *Sci. Remote Sens.* 4, 100034. doi:10.1016/j.srs.2021.100034

Sullivan, M. J., Lewis, S. L., Hubau, W., Qie, L., Baker, T. R., Banin, L. F., et al. (2018). Field methods for sampling tree height for tropical forest biomass estimation. *Methods Ecology Evolution* 9, 1179–1189. doi:10.1111/2041-210x.12962

Tang, H., Stoker, J., Luthcke, S., Armston, J., Lee, K., Blair, B., et al. (2023). Evaluating and mitigating the impact of systematic geolocation error on canopy height measurement performance of GEDI. *Remote Sens. Environ.* 291, 113571. doi:10.1016/j.rse.2023.113571

Tao, S., Guo, Q., Li, C., Wang, Z., and Fang, J. (2016). Global patterns and determinants of forest canopy height. *Ecology* 97, 3265–3270. doi:10.1002/ecy.1580

Tolan, J., Yang, H.-I., Nosarzewski, B., Couairon, G., Vo, H. V., Brandt, J., et al. (2024). Very high resolution canopy height maps from RGB imagery using self-supervised vision transformer and convolutional decoder trained on aerial lidar. *Remote Sens. Environ.* 300, 113888. doi:10.1016/j.rse.2023.113888

Torres, R., Snoeij, P., Geudtner, D., Bibby, D., Davidson, M., Attema, E., et al. (2012). GMES Sentinel-1 mission. *Remote Sensing Environment* 120, 9–24. doi:10.1016/j.rse.2011.05.028

Valentini, R., Arneth, A., Bombelli, A., Castaldi, S., Cazzolla Gatti, R., Chevallier, F., et al. (2014). A full greenhouse gases budget of Africa: synthesis, uncertainties, and vulnerabilities. *Biogeosciences* 11, 381–407. doi:10.5194/bg-11-381-2014

Vancutsem, C., Achard, F., Pekel, J.-F., Vieilledent, G., Carboni, S., Simonetti, D., et al. (2021). Long-term (1990–2019) monitoring of forest cover changes in the humid tropics. *Sci. Advances* 7, eabe1603. doi:10.1126/sciadv.abe1603

Wagner, F. H., Dalagnol, R., Carter, G., Hirye, M., Gill, S., Takougoum, L. B. S., et al. (2025). *High resolution tree height mapping of the amazon forest using planet NICFI images and LiDAR-Informed U-Net model*. arXiv preprint arXiv: 2501.10600.

Wan, L., Ryu, Y., Dechant, B., Hwang, Y., Feng, H., Kang, Y., et al. (2024). Correcting confounding canopy structure, biochemistry and soil background effects improves leaf area index estimates across diverse ecosystems from Sentinel-2 imagery. *Remote Sens. Environ.* 309, 114224. doi:10.1016/j.rse.2024.114224

Wang, Y., Li, G., Ding, J., Guo, Z., Tang, S., Wang, C., et al. (2016). A combined GLAS and MODIS estimation of the global distribution of mean forest canopy height. *Remote Sens. Environment* 174, 24–43. doi:10.1016/j.rse.2015.12.005

Wang, Y., Lehtomäki, M., Liang, X., Pyörälä, J., Kukko, A., Jaakkola, A., et al. (2019). Is field-measured tree height as reliable as believed–A comparison study of tree height estimates from field measurement, airborne laser scanning and terrestrial laser scanning in a boreal forest. *ISPRS Journal Photogrammetry Remote Sensing* 147, 132–145. doi:10.1016/j.isprsjprs.2018.11.008

Xu, L., Saatchi, S. S., Shapiro, A., Meyer, V., Ferraz, A., Yang, Y., et al. (2017). Spatial distribution of carbon stored in forests of the democratic republic of Congo. *Sci. Rep.* 7, 15030. doi:10.1038/s41598-017-15050-z

Xu, L., Saatchi, S. S., Yang, Y., Yu, Y., Pongratz, J., Bloom, A. A., et al. (2021). Changes in global terrestrial live biomass over the 21st century. *Sci. Adv.* 7, eabe9829. doi:10.1126/sciadv.abe9829

Yang, H., Ciais, P., Frappart, F., Li, X., Brandt, M., Fensholt, R., et al. (2023). Global increase in biomass carbon stock dominated by growth of northern young forests over past decade. *Nat. Geosci.* 16, 886–892. doi:10.1038/s41561-023-01274-4

Ygorra, B., Frappart, F., Wigneron, J.-P., Moisy, C., Catry, T., Baup, F., et al. (2021). Monitoring loss of tropical forest cover from Sentinel-1 time-series: a CuSum-based approach. *Int. Journal Applied Earth Observation Geoinformation* 103, 102532. doi:10.1016/j.jag.2021.102532

Zhao, Z., Ciais, P., Wigneron, J.-P., Santoro, M., Brandt, M., Kleinschroth, F., et al. (2024). Central African biomass carbon losses and gains during 2010-2019. *One Earth* 7, 506–519. doi:10.1016/j.oneear.2024.01.021

Zhu, X., Nie, S., Wang, C., Xi, X., Lao, J., and Li, D. (2022). Consistency analysis of forest height retrievals between GEDI and ICESat-2. *Remote Sens. Environ.* 281, 113244. doi:10.1016/j.rse.2022.113244